nature chemical biology

Article

https://doi.org/10.1038/s41589-026-02195-0

Development of a clinically viable MRGPRX4 inverse agonist for cholestatic itch treatment

Received: 21 July 2025

Accepted: 9 March 2026

Published online: 09 April 2026

Check for updates

Jun Yang[1,2,8], Ruichao Shen[3,8], Chunyu Wang[4,8], Wenneng Zhu[1,2], Han Ke[1], Junping Fan[1], Mengna Zhang[5], Yingjun Liu[3], Shuai Li[3], Guochuan Li[3], Xiaoming Wang[3], Yulong Li[2,3,6,7], Can Cao[4,5] ✉ & Xiaoguang Lei[1,2,3] ✉

Chronic itch, particularly in cholestatic and uremic conditions, poses a notable clinical burden, yet treatment options remain inadequate. MRGPRX4 (hX4), a bile-acid-sensing G-protein-coupled receptor predominantly expressed in human sensory neurons, has emerged as a critical mediator of cholestatic pruritus. Here we identified and characterized HEP-50768, a potent and selective small-molecule inverse agonist of hX4 through high-throughput screening and structure–activity optimization. Structural elucidation through cryo-electron microscopy of the hX4–inverse agonist complex structure revealed the unique binding mode and inhibitory mechanism of HEP-50768. In hX4-humanized rats, HEP-50768 robustly suppressed bile-acid-induced pruritic behaviors. Comprehensive preclinical absorption, distribution, metabolism, excretion and safety profiling was performed in both rats and monkeys, and these findings establish HEP-50768 as a promising therapeutic candidate for chronic itch, supporting its advancement to clinical evaluation.

Chronic itch is a pervasive and debilitating condition that severely compromises quality of life and poses a notable unmet medical need. Unlike acute itch, which serves as a protective response, chronic itch persists for weeks or months in the absence of external stimuli and is frequently refractory to conventional antihistamines or corticosteroids. It commonly arises in the context of systemic diseases, including cholestasis[1,2], kidney dysfunction[3,4] and neuropathic disorders[5], yet its molecular mechanisms remain poorly understood. This gap has hindered the development of effective therapeutics, leaving many persons without meaningful relief.

Recent advances have implicated the MRGPRX4 (hX4), predominantly expressed in human sensory neurons[6,7], as a critical mediator of cholestatic pruritus[8–10]. Bile acids, particularly 3-hydroxyl-sulfated derivatives that accumulate in cholestatic conditions, such as primary biliary cholangitis[11] and intrahepatic cholestasis of pregnancy[12], directly activate hX4 to drive itch signaling[8,9,13]. Certain phosphate-containing drugs also induce pruritus through hX4 (ref. 14). Unlike histaminergic pathways, hX4 represents a distinct mechanism linking hepatic or biliary dysfunction to itch. Current treatments[15] including ursodeoxycholic acid[16], maralixibat[17] and rifampin[18] offer limited relief, underscoring the need for targeted interventions.

Therapeutic targeting of hX4 has been challenging because of the absence of potent, selective antagonists or inverse agonists. Given that G-protein-coupled receptors (GPCRs) are among the most druggable targets in the human genome, accounting for 30% of approved therapeutics[19–21], hX4 represents a promising candidate for

[1]Beijing National Laboratory for Molecular Sciences, Key Laboratory of Bioorganic Chemistry and Molecular Engineering of the Ministry of Education, College of Chemistry and Molecular Engineering, New Cornerstone Science Laboratory, Peking University, Beijing, China. [2]Peking-Tsinghua Center for Life Sciences, Academy for Advanced Interdisciplinary Studies, Peking University, Beijing, China. [3]Hepaitech (Beijing) Biopharma Technology Co., Ltd., Beijing, China. [4]Insitute of Health and Medicine, Hefei Comprehensive National Science Center, Hefei, China. [5]National Key Laboratory of Immune Response and Immunotherapy, Center for Advanced Interdisciplinary Science and Biomedicine of IHM, Division of Life Sciences and Medicine, University of Science and Technology of China, Hefei, China. [6]State Key Laboratory of Membrane Biology, School of Life Sciences, Peking University, Beijing, China. [7]PKU-IDG/McGovern Institute for Brain Research, New Cornerstone Science Laboratory, Beijing, China. [8]These authors contributed equally: Jun Yang, Ruichao Shen, Chunyu Wang. ✉e-mail: caocan23@ustc.edu.cn; xglei@pku.edu.cn

https://doi.org/10.1038/s41589-026-02195-0

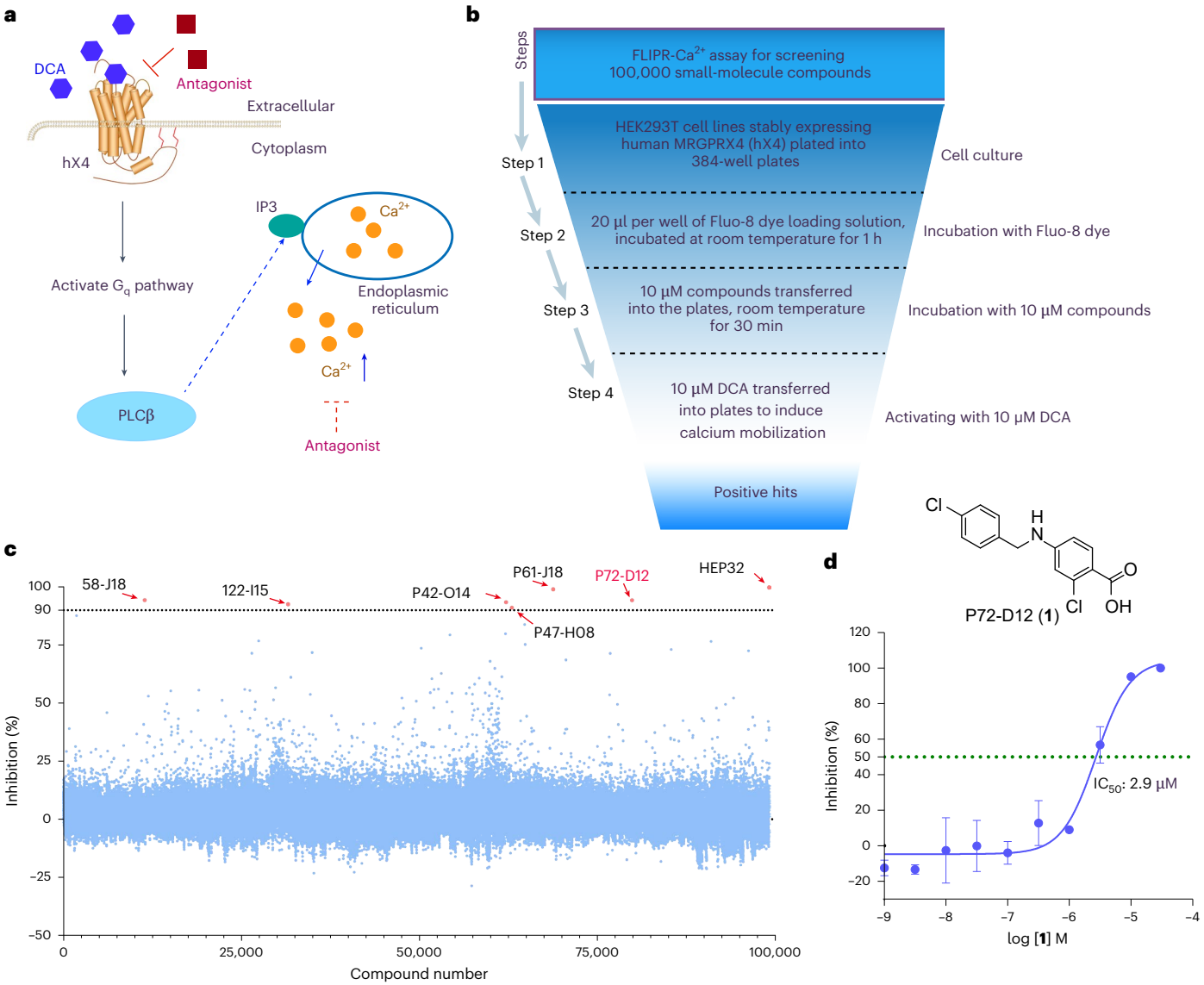

Fig. 1 | High-throughput screening of hX4 antagonists using a FLIPR-Ca^{2+} assay. a, Schematic diagram of screening hX4 antagonists using calcium mobilization assay. DCA activates hX4 through the G_q signaling pathway, triggering calcium mobilization, which can be blocked by antagonists. **b**, Workflow of the FLIPR-Ca^{2+}-based high-throughput screen. HEK293T cells stably expressing hX4 were preincubated with 10 µM of compounds for 30 min, followed by stimulation with 10 µM DCA. **c**, Summary of inhibitory activity from a 100,000-compound screen. Compounds exhibiting >90% inhibition of DCA-induced calcium signals are highlighted in red. **d**, Dose-dependent inhibition of hX4 by hit compound P72-D12. All plots are representative of three biologically independent experiments, with each experimental data point collected with three technical replicates. Data are shown as the mean ± s.e.m.

pharmacologic intervention. Here, we report the discovery and comprehensive characterization of a potent and selective inverse agonist of hX4 identified through high-throughput screening of over 100,000 compounds and the subsequent medicinal chemistry optimization. We solved the cryo-electron microscopy (cryo-EM) structure of hX4 bound to the inverse agonist, revealing its unique molecular mechanism of receptor inhibition, and demonstrated its robust antipruritic efficacy in hX4-humanized rat models, along with favorable absorption, distribution, metabolism, excretion (ADME) and safety profiles. These findings establish this inverse agonist as a promising preclinical candidate for clinical evaluations in cholestatic and other forms of chronic itch.

Results

High-throughput screening to identify hX4 antagonists

Given the critical role of hX4 in mediating cholestatic and other forms of chronic itch, the identification of potent antagonists or inverse agonists marks a pivotal step toward establishing hX4 as a therapeutic target. As a G_q-coupled receptor, hX4 initiates the classical phospholipase C pathway upon activation, elevating inositol triphosphate levels and triggering calcium release from the endoplasmic reticulum into the cytoplasm[8,9,22] (Fig. 1a). This intracellular calcium mobilization serves as a universal downstream readout for G_q-coupled receptor activity.

To explore this mechanism for high-throughput screening, we used a fluorometric imaging plate reader (FLIPR), a well-established fluorescence-based method for detecting intracellular calcium flux[23], which has been widely used in the identification of both agonists and antagonists targeting GPCRs and ion channels[24–26]. In our system, we used deoxycholic acid (DCA), a potent endogenous agonist of hX4, to induce calcium mobilization through the G_q pathway[8,9,13]. In the presence of a functional antagonist or inverse agonist, DCA-induced calcium influx is attenuated, reflected as a reduction in fluorescence intensity in the FLIPR assay (Fig. 1a).

Leveraging this principle, we developed a calcium-based FLIPR screening strategy to identify inhibitors of hX4 activity (Fig. 1b).

https://doi.org/10.1038/s41589-026-02195-0

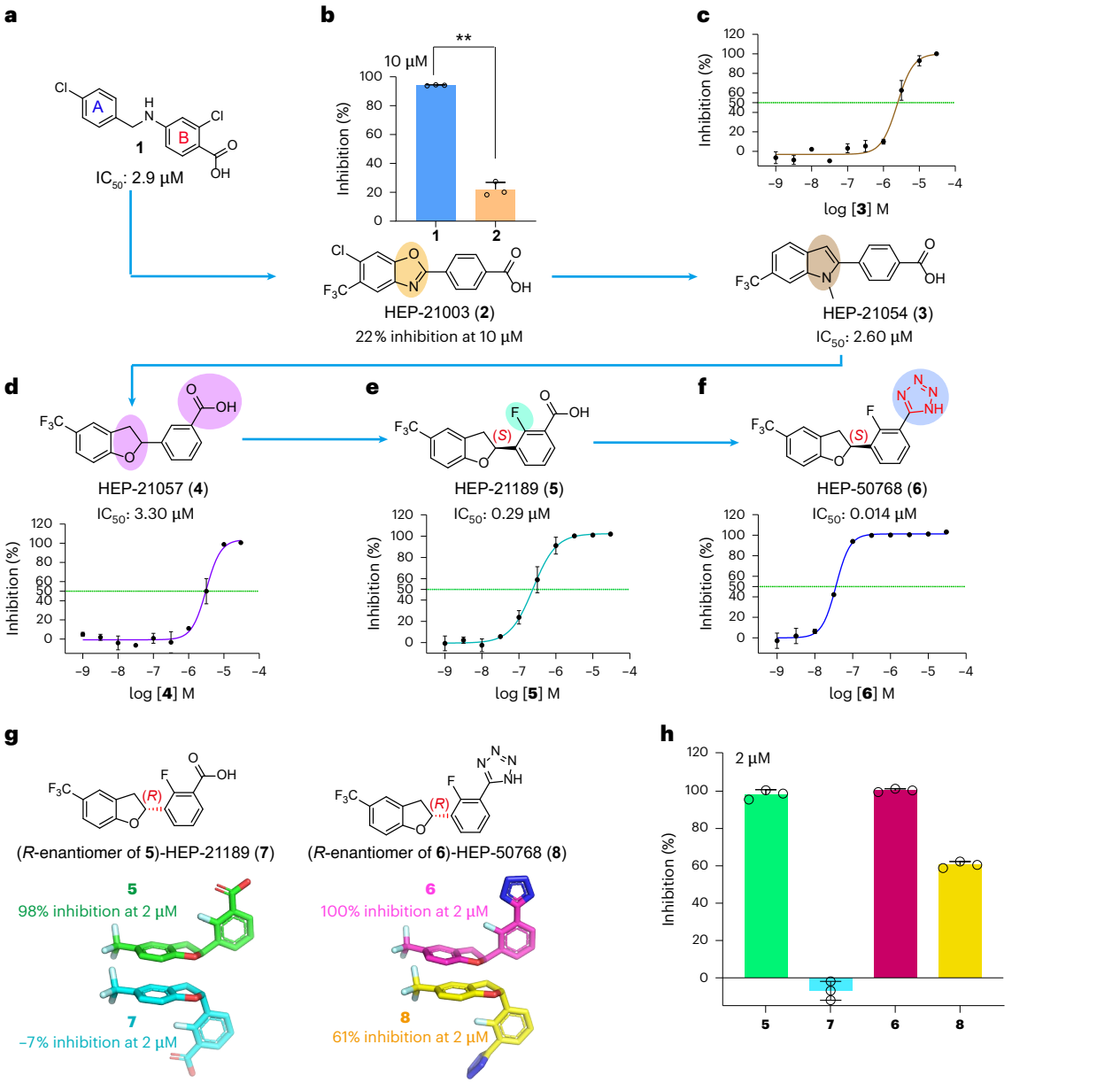

Fig. 2 | SAR-guided optimization of P72-D12 led to the discovery of the potent hX4 antagonist HEP-50768. a, Chemical structure and IC_{50} of the initial compound P72-D12, which features two aromatic moieties: ring A and ring B. **b**, Cyclization of ring A with the adjacent nitrogen (HEP-21003) markedly reduced activity. HEP-21003 showed weak activity at 10 μM. Data were statistically analyzed using an unpaired *t*-test. $^{**}P < 0.001$. **c**, Substitution of the benzoxazole ring with *N*-methylindole yielded HEP-21054, with an IC_{50} of 2.6 μM. **d**, Replacement with a dihydrobenzofuran scaffold produced HEP-21057, which showed an IC_{50} of 3.3 μM. **e**, HEP-21189 with (*S*)-configuration exhibited enhanced potency. **f**, Substitution of the carboxylic acid group with a tetrazole generated HEP-50768, a highly potent hX4 antagonist. **g**, Chemical structures of the (*R*)-enantiomers of HEP-21189 and HEP-50768 (**7** and **8**). The orientation of ring B differs between enantiomers, with the (*S*)-enantiomer pointing upward, correlating with higher potency. **h**, Comparative potency of HEP-21189 (**5**) and HEP-**5**0768 (**6**) and their enantiomers (**7** and **8**) at 2 μM. All plots are representative of three biologically independent experiments, with each experimental data point collected with three technical replicates. Data are shown as the mean ± SEM.

HEK293T cells stably expressing hX4 were preincubated with 10 μM of individual test compounds, followed by stimulation with 10 μM DCA. Using this approach, we screened an in-house chemical library comprising 100,000 structurally diverse small molecules (Supplementary Table 1). From this screen, we identified seven hits that exhibited greater than 90% inhibition of DCA-induced calcium signaling at 10 μM (Fig. 1c and Supplementary Data 1), suggesting robust inhibitory activity against hX4. Of the seven initial hits identified, 58-J18 and HEP32 failed to validate upon resynthesis and retesting. The half-maximal inhibitory concentration (IC_{50}) values of the remaining five hits were as follows: P122-I15 (>10 μM), P47-H08 (3.2 μM), P61-J18 (1.8 μM), P42-O14 (10.6 μM) and P72-D12 (**1**) (2.9 μM) (Fig. 1d and Supplementary Fig. 1). Following the main criteria that the lead compound should be characterized by structure simplicity and tolerability to modification, we selected P72-D12 as a lead candidate for subsequent structure–activity relationship (SAR) studies aimed at optimizing potency, selectivity and pharmacological properties for further drug development.

Optimizing P72-D12 yields a potent hX4 inverse agonist

Given the moderate inhibitory potency of the initial screening hit P72-D12 (IC_{50} = 2.9 μM), we pursued an SAR campaign to develop

analogs with enhanced activity against hX4. Our initial efforts focused on systematic modifications of the two aromatic regions (designated ring A and ring B) of P72-D12 (Fig. 2a).

A cyclization strategy that tethered ring A to the nitrogen represented by the benzoxazole scaffold led to a pronounced loss of activity[27]. For example, compound HEP-21003 (**2**), incorporating this benzoxazole moiety, displayed only 22% inhibition at 10 µM, a significant reduction compared to more than 90% inhibition observed with the parent P72-D12 (Fig. 2b). This loss highlighted the sensitivity of hX4 activity to heteroatoms and conformational constraints in this region. In contrast, replacing the benzoxazole with a *N*-methylindole core, while maintaining the trifluoromethyl group at the 6-position, restored antagonist potency. The resulting analog, HEP-21054 (**3**), exhibited an IC_{50} of 2.6 µM, which is comparable to that of the parent compound, P72-D12 (Fig. 2c). Further modifications to the substitution groups on the indole nitrogen were tolerated, yielding analogs with IC_{50} values ranging from 1 to 4 µM (ref. 27), suggesting some degree of flexibility at this position.

Substitution of indole with benzofuran or indoline resulted in a marked reduction in activity[27], underscoring the structural requirements for optimal receptor interaction. However, replacement with a dihydrobenzofuran scaffold yielded a new series of active compounds[27], including HEP-21057 (**4**), which exhibited an IC_{50} of 3.3 µM (Fig. 2d). Within this scaffold class, SAR analysis revealed two critical features for maintaining potency: the carboxylic acid at the *meta*-position of ring B and the trifluoromethyl group at the 5-position of the dihydrobenzofuran ring. Alterations of the position or nature of these substituents generally diminished activity[27].

Further optimization centered on enhancing molecular interactions and incorporating enantioselectivity. Introduction of a fluorine atom between the carboxylic acid and the dihydrobenzofuran ring on ring B, followed by enantiomeric separation, led to the discovery of HEP-21189 (**5**), an (*S*)-enantiomer with significantly improved potency (Fig. 2e). Modification at the 2-position or 3-position of the dihydrobenzofuran or expansion into a benzopyran scaffold did not yield more active analogs[27].

A key breakthrough was achieved by applying a bioisosteric replacement strategy, in which the carboxylic acid was replaced with a tetrazole moiety. This modification led to the discovery of a new generation of highly potent hX4 antagonists, including HEP-50768 (**6**), which achieved an IC_{50} of 14 nM, approximately 20-fold more potent than HEP-21189 (Fig. 2f). As expected, this enhanced potency was enantioselective; HEP-21189 with the (*S*)-configuration exhibited more than 90% inhibition of DCA-3P-induced calcium mobilization, while the (*R*)-enantiomer (**7**) was inactive at concentrations up to 2 µM (Fig. 2g,h). Similarly, HEP-50768 with the (*S*)-configuration demonstrated significantly greater inhibitory activity than its (*R*)-enantiomer (**8**) (Fig. 2g,h), reinforcing the stereoselective nature of hX4 recognition.

In summary, our SAR-guided optimization of P72-D12 yielded a structurally refined and stereoselective hX4 inhibitor, HEP-50768, with an IC_{50} of 14 nM. This compound is a compelling candidate for further pharmacological development to target chronic itch mediated by hX4.

HEP-50768 is a potent and selective inverse agonist of hX4

Having identified HEP-50768 as a highly potent antagonist of hX4, we next sought to elucidate its molecular mechanism of inhibition. A detailed understanding of how HEP-50768 modulates hX4 activity is essential for validating its pharmacological profile and guiding the rational design of next-generation antagonists. We initially assessed the basal activity of hX4 by quantifying intracellular inositol monophosphate (InsP) in HEK293T cells expressing hX4. In the absence of exogenous hX4 agonists, hX4-expressing cells exhibited approximately 58% higher basal InsP levels compared to parental HEK293T controls, indicating substantial constitutive activity of the receptor. Treatment with HEP-50768 or compound 1-55, an antagonist of hX4 disclosed in a patent[28], significantly reduced basal InsP production (Fig. 3a), suggesting that HEP-50768 and 1-55 function as inverse agonists, actively suppressing the receptor's intrinsic activity rather than merely blocking agonist-induced signaling. Notably, HEP-50768 exhibited comparable inhibition to DCA and DCA-3P-induced signaling changes and revealed greater efficacy than 1-55 (Fig. 3b). Importantly, HEP-50768 exhibited minimal cross-reactivity with other itch-associated MRGPRX family members. Specifically, it showed only weak inhibition of MRGPRX1 (hX1) with an IC_{50} of 16 µM and MRGPRX2 (hX2) with an IC_{50} of 1.5 µM (Fig. 3c and Supplementary Fig. 2). Moreover, HEP-50768 did not activate either hX1 or hX2 (Fig. 3d and Supplementary Fig. 2), highlighting its high selectivity for hX4 within the itch-related MRGPRX subfamily of receptors.

HEP-50768 interacts with hX4 in its G-protein-bound form

To gain deeper insight into the molecular basis of HEP-50768 inhibition, we sought to determine the structure of the hX4–HEP-50768 complex in its inactive state. Multiple strategies were tested, including insertion of a thermostabilizing BRIL fusion into intracellular loop 3 (ICL3) for complexation with anti-BRIL Fab[29] and replacement of ICL3 to facilitate nanobody (Nb6 or Mb6)[30] binding. However, none of these approaches yielded a sufficiently stable complex for high-resolution structure determination. This difficulty likely arises from the intrinsically basal activity of hX4, which prevents it from adopting a stable inactive conformation. Although inverse agonists are traditionally thought to stabilize GPCRs in G-protein-free inactive states, recent work has demonstrated that specific inverse agonists, such as those targeting the κ-opioid receptor, can also capture receptor–G protein complexes[31]. While such states are transient in vivo because of GDP rebinding to the G protein, they can be stabilized experimentally.

To assess functional coupling between purified hX4 and $G\alpha_q$, we performed GTP turnover experiments. In the absence of ligands (apo), increasing hX4 concentrations led to enhanced GTP hydrolysis (Fig. 3e), confirming its intrinsic basal activity. The addition of DCA-3P further increased while HEP-50768 reduced GTPase activity relative to the apo state (Fig. 3e), suggesting that hX4 remains capable of engaging the G protein in both the absence and the presence of inverse agonist. Given that mini$G\alpha_q$, which lacks the α-helical domain and GDP-binding capacity, has been widely used to stabilize GPCR–G protein complexes, we next examined whether hX4 could form a stable complex with mini$G\alpha_q$ protein without an agonist. Using the baculovirus expression system, we successfully coexpressed and purified hX4–mini$G\alpha_q$ complexes (Extended Data Fig. 1a). Notably, hX4 robustly assembled with mini$G\alpha_q$ protein even without activating ligand, consistent with its substantial basal signaling activity (Fig. 3a). To confirm direct binding, surface plasmon resonance (SPR) experiments were conducted using purified apo hX4 and hX4–mini$G\alpha_q$ protein complexes. HEP-50768 bound both forms with comparable affinity, with equilibrium dissociation constants (K_D) of 0.6 nM and 0.7 nM, respectively (Extended Data Fig. 1b,c), demonstrating that HEP-50768 can engage hX4 irrespective of its G-protein-coupling state.

Structural insights into HEP-50768 inhibiting hX4

To elucidate the molecular mechanism by which HEP-50768 inhibits hX4, using single-particle cryo-EM, we solved the structure of HEP-50768-bound hX4 in complex with miniG_q protein at a global resolution of 2.63 Å (Fig. 3f, Extended Data Fig. 2a–c and Supplementary Table 2), with local refinement yielding a 2.56-Å map for the receptor (Extended Data Fig. 2d,e and Supplementary Table 2). Both the overall resolution and the map quality were better than our previously determined agonist-bound hX4–G protein complex structures[13,14,24]. The well-resolved density for ligand and transmembrane helices enabled confident modeling of HEP-50768 and the surrounding residues (Fig. 3g and Extended Data Fig. 2f,g).

The overall architecture of the HEP-50768-bound hX4 complex ($hX4^{HEP\text{-}50768}$) closely resembled that of previously reported agonist-bound structures, with only subtle conformational changes observed in the G

https://doi.org/10.1038/s41589-026-02195-0

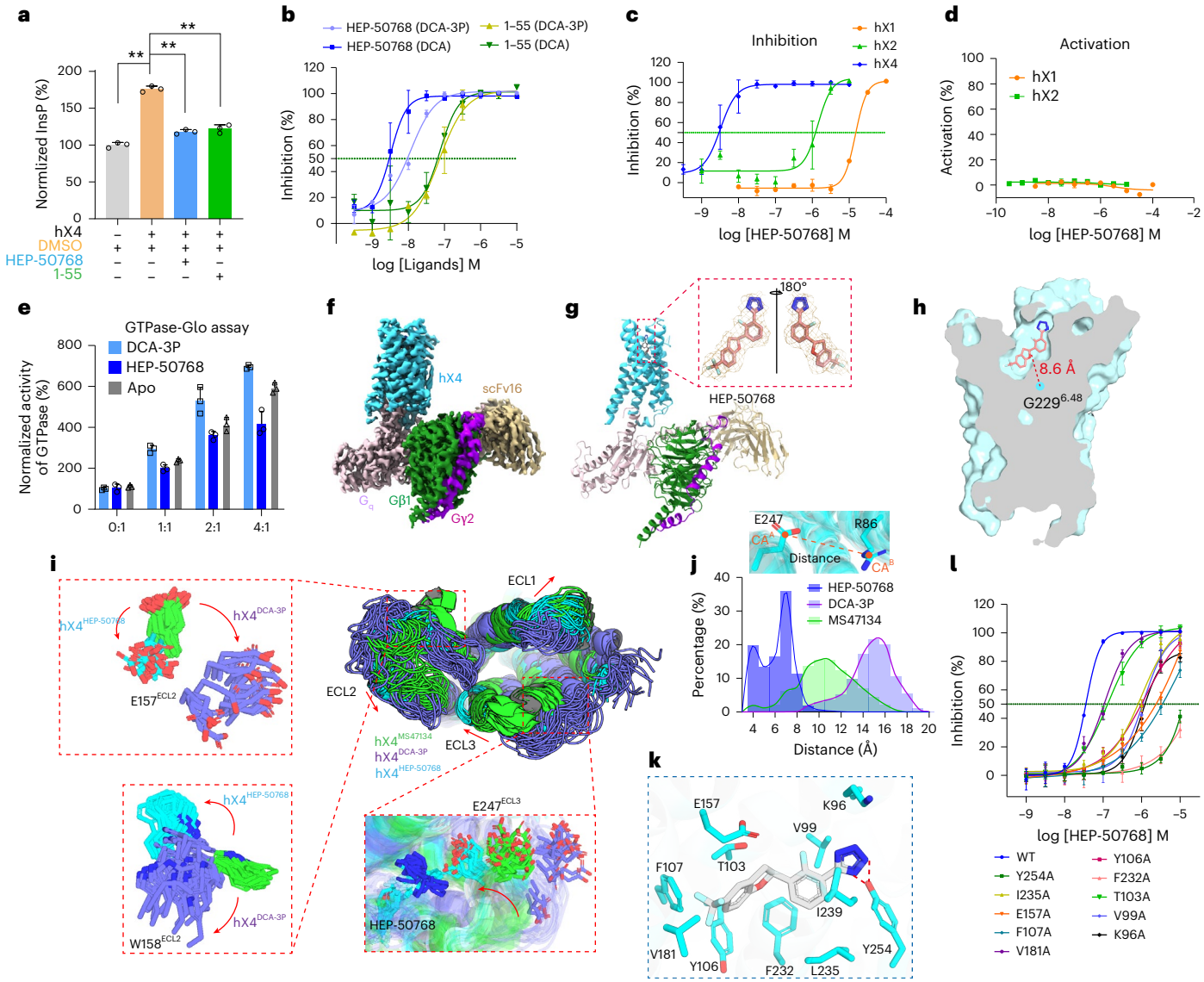

Fig. 3 | Structural insights into the inverse agonist HEP-50768 bound to hX4. **a**, HEP-50768 and 1-55 reduced basal hX4 activity, measured by intracellular InsP levels in HEK293T cells expressing hX4. Basal InsP was suppressed by 0.1 μM HEP-50768 or 1-55, confirming inverse agonism. Data are shown as the mean ± s.e.m. Data were statistically analyzed using a two-sided unpaired *t*-test. $^{**}P < 0.001$. **b**, Dose-dependent inhibition of Ca^{2+} mobilization by HEP-50768 or 1-55 upon DCA-3P or DCA stimulation. **c**,**d**, Activity of HEP-50768 toward MRGPRX1 (hX1) and MRGPRX2 (hX2): inhibition (**c**) and activation (**d**). **e**, GTPase-Glo assay of recombinant hX4–G_q in detergent micelles. Increasing hX4:G_q ratios elevated GTP hydrolysis; DCA-3P further increased while HEP-50768 modestly decreased turnover rates. **f**,**g**, Cryo-EM structure of the $hX4^{HEP\text{-}50768}$–miniGα_q complex. The density map (**f**) and overall structure (**g**) show hX4 (cyan), G_q (pink), Gβ1 (green), Gγ2 (purple) and scFv16 (yellow). The well-resolved ligand density allowed precise placement of HEP-50768. **h**, HEP-50768 binds approximately 8.6 Å from $G229^{6.48}$, a position analogous to the toggle-switch $W^{6.48}$ in other GPCRs. The ligand is shown as pink sticks; the receptor is shown in surface representation. **i**, Overlaid MD trajectory of $hX4^{HEP\text{-}50768}$ (cyan), $hX4^{MS47134}$ (green) and $hX4^{DCA\text{-}3P}$ (purple). Agonist-bound and inverse-agonist-bound states exhibit distinct conformations in ECL1–ECL3. $E157^{ECL2}$ and $W158^{ECL2}$ adopt divergent orientations and E247 moves inward to cap the pocket in $hX4^{HEP\text{-}50768}$. **j**, Distance between E247 and R86 during MD simulations for the three complexes. **k**, Detailed ligand–receptor interactions. HEP-50768 (silver, sticks) forms extensive hydrophobic interactions with surrounding residues (cyan, sticks), while Y254 forms polar interactions with the tetrazole moiety. Polar interactions are shown as red dashed lines. **l**, Alanine substitutions of key residues reduced antagonist potency. All panels represent three biologically independent experiments, each with three technical replicates. Data are shown as the mean ± s.e.m.

protein (Extended Data Fig. 3a). The intracellular regions remained similar to MS47134-bound ($hX4^{MS47134}$), fospropofol-bound ($hX4^{fospropofol}$) and DCA-3P-bound hX4 ($hX4^{DCA\text{-}3P}$), while the extracellular domains of hX4, particularly extracellular loop 1 (ECL1), ECL2 and ECL3, underwent notable rearrangements (Extended Data Fig. 3b).

Within the ligand-binding pocket, HEP-50768 adopts a deeply buried position within the transmembrane core, in contrast to the more surface-exposed binding poses of agonists such as MS47134 (ref. 24) and fospropofol[14] (Extended Data Fig. 4a). Its orientation resembles that of DCA-3P (ref. 13), which also binds close to $G229^{6.48}$, the residue corresponding to the toggle residue $W^{6.48}$ in family A GPCRs[32] (Fig. 3h, Extended Data Fig. 4a and Supplementary Fig. 3a). Substitution of $G229^{6.48}$ to tryptophan abolished both basal and DCA-induced activity, highlighting its essential role in hX4 activation (Supplementary Fig. 3b,c). Compared to $hX4^{MS47134}$ and $hX4^{fospropofol}$, binding of HEP-50768 induces substantial rearrangement of residues $W158^{ECL2}$ and $E157^{ECL2}$, which shift outward 7.2 Å and 3.4 Å, respectively, to accommodate the ligand (Extended Data Fig. 4b). Compared to $hX4^{DCA\text{-}3P}$, these residues also displayed conformational changes (Extended Data Fig. 4c). To probe these conformational differences,

https://doi.org/10.1038/s41589-026-02195-0

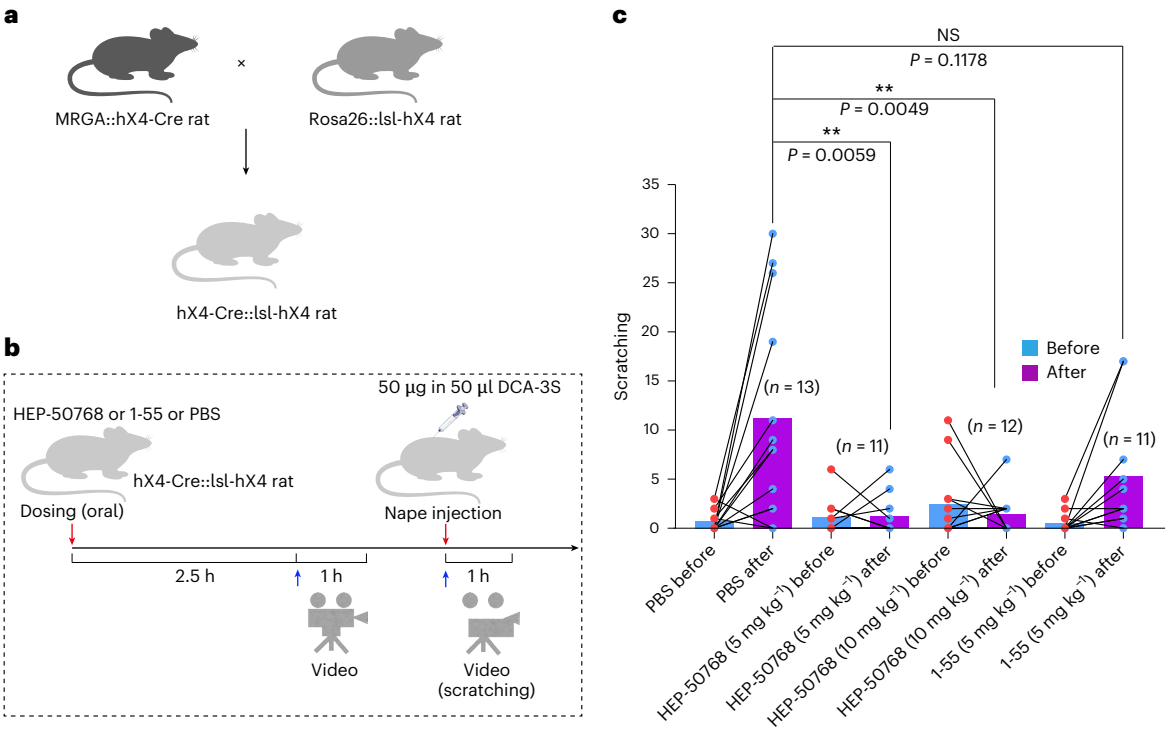

Fig. 4 | HEP-50768 alleviates DCA-3S-induced pruritus in an hX4-humanized rat model. a, Schematic illustration of the generation of hX4-humanized rats used for behavioral studies. **b**, Experimental procedure for assessing the anti-itch efficacy of HEP-50768. hX4-humanized rats were orally administered 5 and 10 mg kg^{-1} HEP-50768 or 5 mg kg^{-1} 1-55 (positive control) or PBS (negative control), followed by intradermal injection of DCA-3S to induce itch. Scratching behavior was recorded for 1 h before DCA-3S injection. Subsequently, 50 µg of DCA-3S in 50 µl was injected into the nape of the neck and scratching behavior was recorded for an additional hour. Scratching bouts were quantified as a measure of pruritus. **c**, HEP-50768 significantly reduced DCA-3S-induced scratching behavior using hX4-humanized rats (n = 11–13 rats per group). Data are shown as the mean ± s.e.m. Data were statistically analyzed using the Mann–Whitney test. NS, not significant. **P < 0.001.

we conducted three independent 100-ns molecular dynamics (MD) simulations of hX4^{MS47134}, hX4$^{DCA\text{-}3P}$ and hX4$^{HEP\text{-}50768}$. All receptor–ligand complexes remained stable (Extended Data Fig. 5a–c) with ligand root-mean-square deviation values below 2 Å (Extended Data Fig. 5d–i), suggesting the stable interactions between ligands and hX4. During the simulations, ECL3 of hX4$^{HEP\text{-}50768}$ folds inward to cap the ligand-binding pocket, whereas, in hX4$^{DCA\text{-}3P}$ and hX4^{MS47134}, ECL3 extends outward toward the solvent (Fig. 3i). ECL1 and ECL2 in hX4$^{HEP\text{-}50768}$ exhibit slight outward and inward displacements, respectively, resembling hX4^{MS47134} relative to hX4$^{DCA\text{-}3P}$ (Fig. 3i). Notably, compared to hX4$^{HEP\text{-}50768}$, E157 and W158 in ECL2 of hX4^{MS47134} and hX4$^{DCA\text{-}3P}$ adopt divergent orientations across the three structures for ligand accommodation (Fig. 3i). Strikingly, E247 in ECL3, solvent exposed in agonist-bound states to permit phosphate group binding, folds inward in hX4$^{HEP\text{-}50768}$, maintaining a distance of 4–7 Å to R86 throughout the simulations, compared to >10 Å in agonist-bound states (Fig. 3i,j). This likely forms a strong interaction with the positively charged residue R86, potentially obstructing access of phosphate or other negatively charged groups essential for many agonists recognition and activation. These observations highlight distinct ECL rearrangements underlying inverse agonist versus agonist binding.

HEP-50768 is tightly nestled in an 'L-shaped' hydrophobic pocket formed by transmembrane domains 3–7 (TM3–TM7) (Extended Data Fig. 4d). This compact configuration explains the strict (*S*)-stereoselectivity of hX4, as the (*R*)-enantiomer of HEP-50768 would clash sterically with adjacent residue V99 (Extended Data Fig. 4e). Multiple hydrophobic residues, such as F107, F232, V99 and I239, stabilize the ligand through van der Waals interactions, while Y254 forms hydrogen bonds with the tetrazole moiety (Fig. 3k). Alanine substitution of these residues significantly reduced the antagonist activity (Fig. 3l, Supplementary Fig. 4 and Supplementary Table 3), confirming their essential roles in stabilizing HEP-50768.

Analysis of conserved GPCR microswitch motifs further clarified the structural basis of inverse agonism. In the CWxP (corresponding to CGxP in hX4) motif, residues C228$^{6.47}$, P231$^{6.50}$ and G229$^{6.48}$ were displaced inward by 1.4–1.5 Å compared to active-state hX4 structures (Extended Data Fig. 6a). In D/ERY (corresponding to ERC in hX4)[33], R120$^{3.50}$ adopted a distinct conformation and formed a hydrogen bond with T221$^{6.40}$, an interaction absent in agonist-bound structures (Extended Data Fig. 6b). The NPxxY motif remained largely unchanged (Extended Data Fig. 6c). These subtle but coordinated rearrangements are consistent with previously described mechanisms in which microswitch distortion leads to decoupling of ligand binding from downstream signaling, resulting in a signaling-silent or inverse-agonist-bound state[31,34].

The constitutive activity of hX4 likely arises from the absence of the canonical TM3–TM6 ionic lock between R$^{3.50}$ and D/E$^{6.30/6.33}$. In hX4, E$^{6.33}$ is occupied by L214$^{6.33}$, which cannot form the stabilizing salt bridge found in the β_2 adrenergic receptor (β_2AR)[35,36] and other aminergic GPCRs (Extended Data Fig. 6d,e). Substitution of L214$^{6.33}$ to glutamic acid abolished the basal activity (Extended Data Fig. 6f), confirming its role in maintaining constitutive activity. Instead, L214$^{6.33}$ engages in favorable hydrophobic interactions with L244 and L245 at the C terminus of the Gα5 helix (Extended Data Fig. 6e), which may facilitate receptor–G protein coupling. Together, these findings provide a comprehensive structural basis of HEP-50768's potent inverse agonist activity and illuminate the molecular features governing hX4's constitutive signaling. These insights provide a structural framework for the rational design of next-generation antipruritic therapeutics targeting hX4.

HEP-50768 alleviates DCA-3S-induced itch in humanized rats

To evaluate the therapeutic potential of HEP-50768 in cholestatic pruritus, we used the hX4-humanized rat model[13], a critical in vivo platform

for assessing hX4-mediated itch (Fig. 4a). HEP-50768 was administered orally at 5 or 10 mg kg^{-1}, with 1-55 (5 mg kg^{-1}) was used as a positive control (Fig. 4b). Then, 3 h after dosing, pruritus was induced through intradermal injection of DCA-3S, a human endogenous 3-sulfated bile acid with high affinity for hX4 (ref. 13) and pruritogenic activity, and scratching bouts were quantified before and after DCA-3S administration as a behavioral readout of itch severity (Fig. 4b). As expected, oral administration of HEP-50768 significantly reduced DCA-3S-induced scratching compared to vehicle-treated controls and 1-55, which showed weaker inhibitory potency toward hX4 and did not show a significant effect at the tested dose (Fig. 4c). These findings establish HEP-50768 as a promising candidate for treating hX4-mediated pruritus and underscore its translational value for managing chronic itch, a condition currently lacking effective targeted therapies.

HEP-50768 pharmacokinetic profile in rats and rhesus monkeys

To characterize the pharmacokinetic (PK) properties of HEP-50768 across species, we conducted comprehensive single-dose and multiple-dose PK studies in Sprague-Dawley (SD) rats and rhesus monkeys following intravenous (i.v.) and oral administration.

After a single i.v. dose of 5 mg kg^{-1} in rats (Extended Data Fig. 7a), HEP-50768 exhibited a mean terminal half-life ($t_{1/2}$) of 6.65 h in males and 6.44 h in females (Extended Data Fig. 7b and Supplementary Data 2). The systemic clearance was approximately 45 ml h^{-1} kg^{-1} (Supplementary Data 2), less than 10% of hepatic blood flow (~3,312 ml h^{-1} kg^{-1}), indicating a low-clearance compound. Following a single oral dose of 5, 15 and 50 mg kg^{-1} (Extended Data Fig. 7c), the time to reach peak plasma concentrations (T_{max}) ranged from 6 to 10 h, except for females at 5 mg kg^{-1}, which reached T_{max} at approximately 2 h (Extended Data Fig. 7d and Supplementary Data 2). Peak concentration (C_{max}) (Extended Data Fig. 7e) and overall exposure (AUC_{last}) (Extended Data Fig. 7f) were comparable between sexes across all tested doses ($P > 0.05$), indicating no sex-related PK differences. HEP-50768 exhibited high absolute bioavailability of 78.86% in males and 79.60% in females at 5 mg kg^{-1} (Extended Data Fig. 7g), suggesting efficient gastrointestinal absorption and minimal first-pass metabolism. Dose proportionality analysis revealed a greater-than-dose-proportional increase in exposure. Although the dose ratios were 1:3:10, the AUC_{last} ratios were 1:4.49:21.98 in males and 1:4.28:25.35 in females (Extended Data Fig. 7h), indicating nonlinear PK. In a 7-day repeated-dosing study (15 mg kg^{-1}, oral), exposures on day 7 were comparable to day 1 (C_{max} ratio of day 7/day 1: 1.41–2.01, AUC_{last} ratio of day 7/day 1: 1.20–1.82) (Extended Data Fig. 7i–k and Supplementary Data 2), demonstrating minimal accumulation with daily administration.

In rhesus monkeys, a single i.v. administration of 2.5 mg kg^{-1} yielded a $t_{1/2}$ of 9.12 h in males and 4.72 h in females (Fig. 5a,b and Supplementary Data 3). Clearance values were again below 10% of hepatic blood flow (~2,616 ml h^{-1} kg^{-1}), confirming a low clearance profile (Supplementary Data 3). Following oral administration at 2.5, 7.5 and 25 mg kg^{-1}, exposure increased more than dose-proportionally (dose ratio: 1:3:10, AUC_{last} ratio: 1:4.39:26.22 for males and 1:5.00:28.76 for females) and sex-related differences in exposure were negligible across oral administration groups ($P > 0.05$) (Fig. 5c–f), likely reflecting saturation of elimination pathways or enhanced absorption at higher doses. Oral bioavailability was unexpectedly high (105.32% in males and 89.22% in females) at the dose of 2.5 mg kg^{-1} (Fig. 5g). Repeated daily dosing at 7.5 mg kg^{-1} for 7 days (Fig. 5h) also revealed no drug accumulation (C_{max} ratio of day 7/day 1: 0.81–1.57, AUC_{last} ratio of day 7/day 1: 1.20–1.70) (Fig. 5i,j), confirming a stable PK profile over time.

HEP-50768 tissue distribution and excretion pathway in rats

To assess the in vivo distribution of HEP-50768, tissue PK were evaluated following a single oral gavage of 5 mg kg^{-1} in SD rats. HEP-50768 was rapidly and extensively distributed, with quantifiable exposure in nearly all examined tissues (Fig. 5k and Supplementary Table 4). The highest AUC_{last} were observed in the liver, followed by the kidney, stomach, small intestine, plasma, large intestine, lung, heart, spleen, ovary, skin, muscle and fat (Fig. 5k). In contrast, HEP-50768 was undetectable in the spinal cord, while brain exposure was negligible (approximately 1% of plasma levels), indicating minimal central nervous system (CNS) penetration (Fig. 5k). Tissue T_{max} varied across organs; most peripheral tissues reached C_{max} at 6 h after administration, whereas stomach and small intestine peaked at 0.5 h, reflecting rapid absorption and gastrointestinal exposure (Supplementary Table 4). These findings confirm that HEP-50768 undergoes rapid and widespread distribution after oral administration, preferentially accumulating in the liver and kidneys while exhibiting restricted CNS exposure, an advantageous feature for a peripherally acting, non-CNS-targeted therapy.

To elucidate the primary elimination pathway, cumulative excretion was quantified in feces, urine and bile over 168 h following a single 5 mg kg^{-1} oral dose in SD rats. HEP-50768 was predominantly excreted in feces, with peak elimination occurring 24–32 h after administration (Fig. 5l). The cumulative fecal excretion of unchanged HEP-50768 was 70.70% in males and 57.00% in females (Fig. 5m). Urinary excretion was negligible (<0.2% of the dose) (Fig. 5l,m), while biliary excretion accounted for 19.85% and 11.98% in males and females, respectively (Fig. 5l,m). Collectively, these data indicate that HEP-50768 is primarily eliminated through hepatobiliary and fecal routes in its parent form, consistent with its low renal clearance and high oral bioavailability.

Moreover, in vitro incubations with primary hepatocytes from mice, rats, dogs, monkeys and humans revealed the high metabolic stability of HEP-50768, with parent compound levels of 90.56%, 96.74%, 98.64%, 71.78% and 98.70%, respectively (Fig. 5n).

Toxicity studies of HEP-50768 in SD rats and rhesus monkeys

A 4-week repeated-dose toxicity study of HEP-50768 was conducted in SD rats (Extended Data Fig. 8a). Animals received HEP-50768 as once-daily oral gavage doses of 6, 20 or 60 mg kg^{-1}. Because of mortality observed at 60 mg kg^{-1}, the high dose was reduced to 50 mg kg^{-1} on day 15 (Extended Data Fig. 8a). Toxicokinetic analyses revealed no significant gender-based differences in C_{max} and AUC_{last} on days 1, 15 and 28 (Extended Data Fig. 8b). After oral gavage administration of HEP-50768 at 6, 20 and 60 or 50 mg kg^{-1} to rats on day 1 and day 28, C_{max} and AUC_{last} increased in a greater-than-dose-proportional manner across the tested dose range (Extended Data Fig. 8b–d). After 28 days of dosing, compared to the first dosing, AUC_{last} ratios (day 28/day 1) at 6 and 20 mg kg^{-1} ranged from 1.85 to 2.18 in both sexes (Extended Data Fig. 8e,f), indicating mild systemic accumulation. In contrast, no accumulation was observed at 50 mg kg^{-1} dose (Extended Data Fig. 8e,f).

To evaluate potential translational relevance, a parallel 4-week repeated-dose toxicity study of HEP-50768 was conducted in rhesus monkeys (Fig. 6a). Monkeys were dosed daily at 5 (low dose), 25 (middle dose) or 120 or 60 mg kg^{-1} (high dose). In the high-dose group, males initially received 120 mg kg^{-1} for 6 days, reduced to 60 mg kg^{-1} from day 7 onward because of early toxicity, while females received 60 mg kg^{-1} throughout (Fig. 6a). Consistent with rat data, toxicokinetic analysis in rhesus monkeys demonstrated C_{max} and AUC_{last} increased with dose and AUC_{last} increased more than proportionally (Fig. 6b and Supplementary Table 5). Exposure ratios (day 28/day 1) ranged from 0.62 to 1.6, demonstrating no significant accumulation following repeated administration (Fig. 6c,d).

HEP-50768 showed no off-target activity and minimal hERG inhibition

To evaluate the pharmacological selectivity of HEP-50768, its activity was profiled against 48 off-target candidates (Supplementary Protocols). At 10 μM, HEP-50768 exhibited no significant agonistic or antagonistic activity (<50% modulation) on 47 of the targets tested, including AGTR1, which often recognizes tetrazole-containing compounds[37] (Fig. 6e and

https://doi.org/10.1038/s41589-026-02195-0

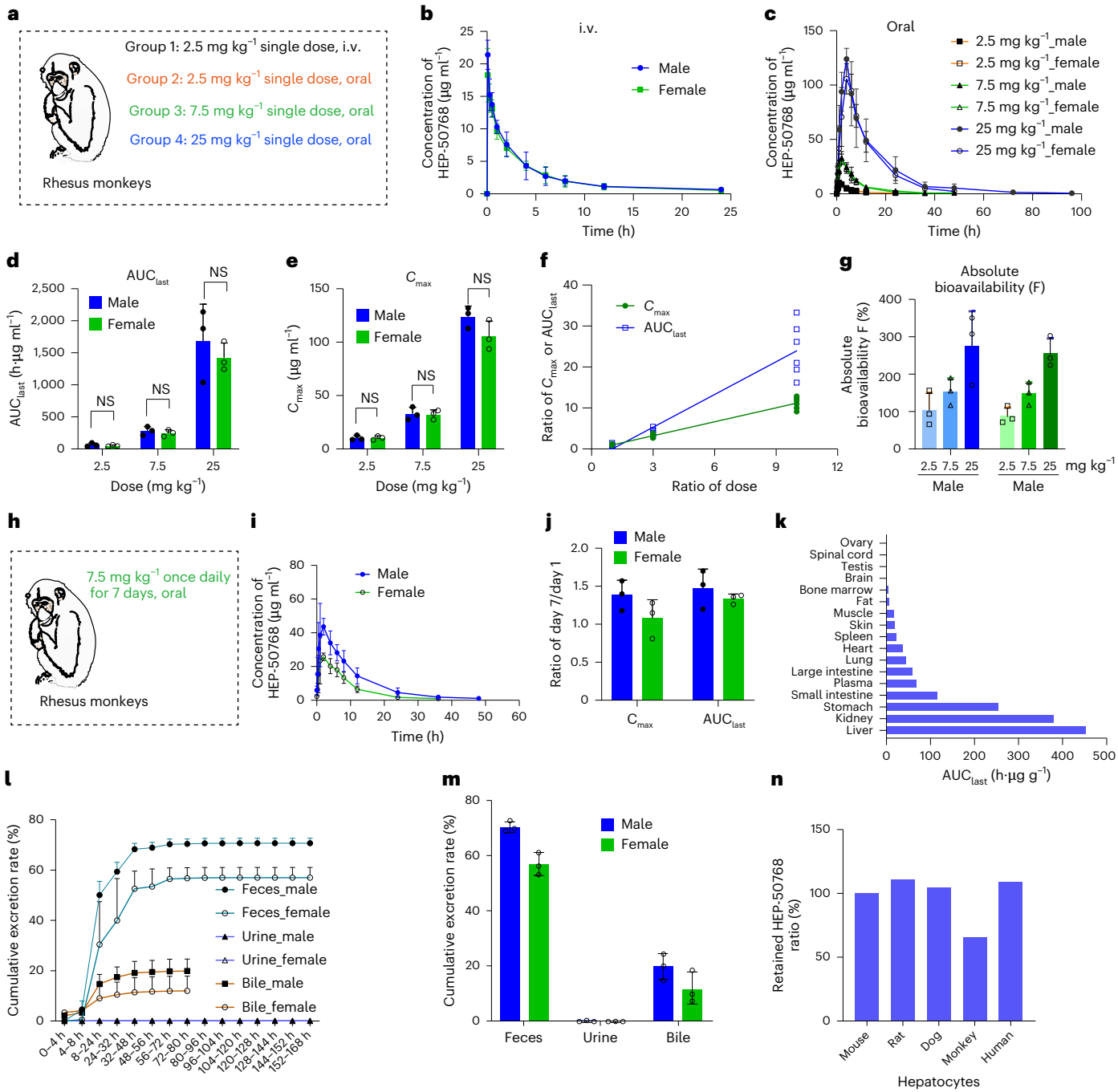

Fig. 5 | PK of HEP-50768 in rhesus monkeys and tissue distribution in rats. **a**, Schematic overview of the PK study design. Rhesus monkeys were divided into four groups. Group 1 received a single i.v. dose of 2.5 mg kg^{-1}, while groups 2–4 received a single oral dose of 2.5, 7.5 and 25 mg kg^{-1}, respectively ($n = 6$ per group; 3 males and 3 females). **b**,**c**, Plasma drug concentration–time profiles following i.v. (**b**) and oral (**c**) administration. **d**,**e**, AUC_{last} (**d**) and C_{max} (**e**). Data were statistically analyzed using a two-sided unpaired *t*-test. **f**, Oral administration of 2.5, 7.5 and 25 mg kg^{-1} resulted in greater-than-dose-proportional increases in both C_{max} and AUC_{last}. **g**, Absolute oral bioavailability of HEP-50768 in rhesus monkeys. **h**, Schematic of the 7-day repeated-dose study in rhesus monkeys. Monkeys received 7.5 mg kg^{-1} HEP-50768 orally once daily. **i**, Day 7 plasma drug concentration–time profile of HEP-50768 following repeated daily dosing at 7.5 mg kg^{-1}. **j**, Comparable C_{max} and AUC_{last} on day 7 and day 1 indicated minimal accumulation upon repeated dosing. **k**, Tissue distribution of HEP-50768 after a single oral dose of 5 mg kg^{-1} in SD rats. The compound was primarily distributed to the liver, kidneys and stomach. The blood and tissue samples were collected at 0.5, 6, 12 and 24 h after administration. **l**, Cumulative excretion rate–time curve of HEP-50768. **m**, Cumulative excretion rate of HEP-50768 through feces, urine and bile. The compound was predominantly excreted in feces, with negligible renal elimination. **n**, Metabolic stability of HEP-50768 in hepatocytes from various species. Data are shown as the mean ± s.e.m. Both male and female rhesus monkeys were included in all groups.

Supplementary Data 4). Although a moderate inhibitory effect was observed for 5-HT_{2B}, subsequent dose–response analysis revealed a plateau in inhibitory activity, with only a minimal increase at 100 μM relative to 10 μM (Fig. 6f), indicating low potency and limited relevance at therapeutic concentrations.

Given the importance of cardiac safety, hERG channel inhibition, which contributes to phase 3 repolarization of the cardiac action potential[38–40], was evaluated using manual patch-clamp electrophysiology in HEK293 cells stably expressing the hERG channels. HEP-50768 demonstrated minimal inhibition, with an IC_{50} exceeding

https://doi.org/10.1038/s41589-026-02195-0

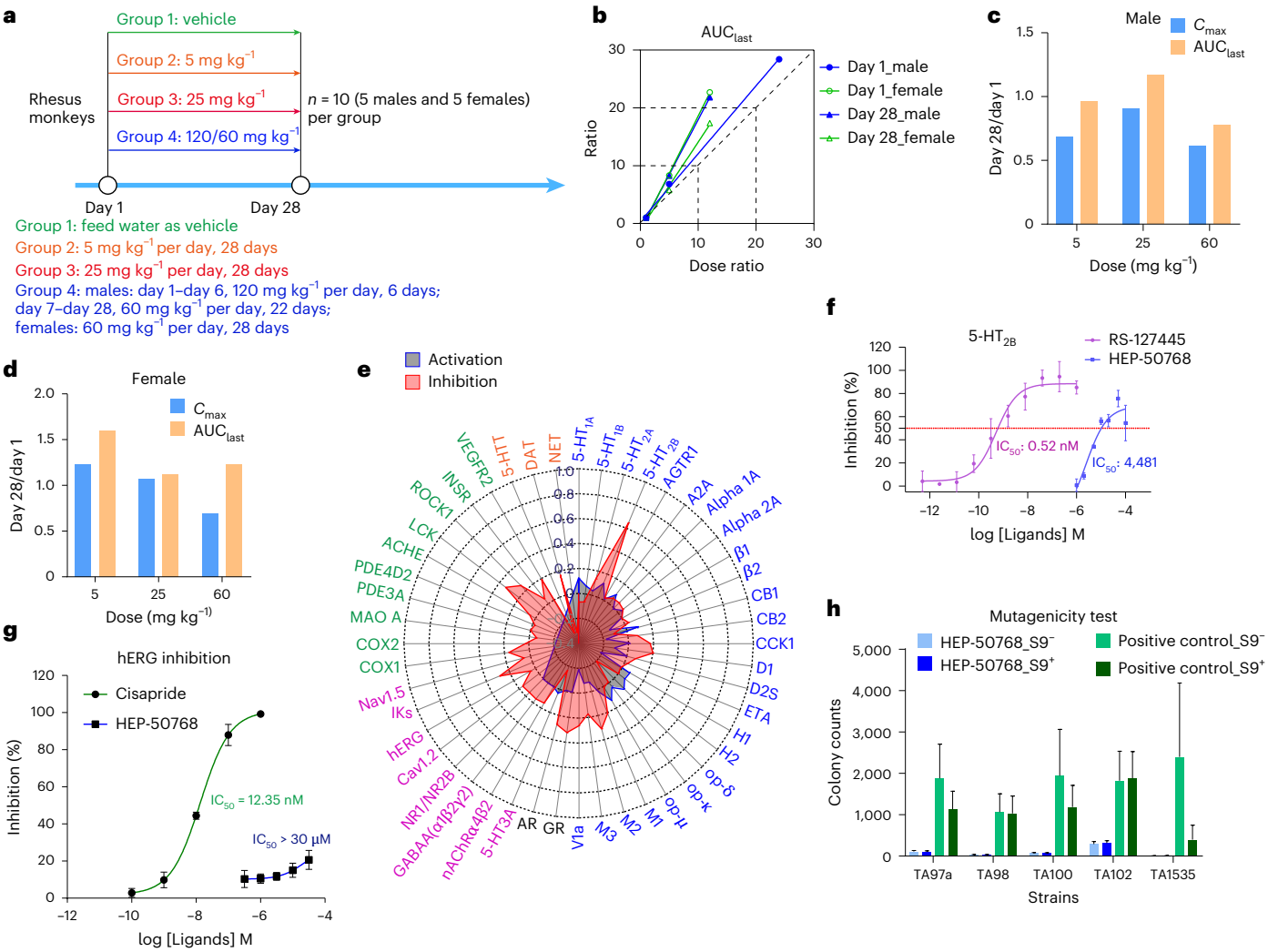

Fig. 6 | Preclinical safety and toxicity assessment of HEP-50768. a, Schematic overview of a 4-week repeated-dose toxicity study of HEP-50768 in rhesus monkeys. Animals were divided into four groups. Group 1 received the vehicle as a control, while groups 2–4 received oral doses of 5 mg kg^{-1} (low dose), 25 mg kg^{-1} (middle dose) and 120 or 60 mg kg^{-1} (high dose), respectively. Both male and female rhesus monkeys were included in all groups ($n = 6$ per group; 3 males and 3 females). **b**, Oral administration of 5, 25 and 120 or 60 mg kg^{-1} resulted in greater-than-dose-proportional increases in AUC_{last} on both day 1 and day 28. **c**,**d**, Comparable C_{max} and AUC_{last} on day 28 versus day 1 in males (**c**) and females (**d**) indicated no accumulation upon repeated dosing. **e**, Safety panel screening of HEP-50768 across 48 targets at 10 μM. HEP-50768 exhibited less than 50% activation and inhibition activity across all targets, except for inhibition of 5-HT_{2B}. Targets included 25 GPCRs (blue), 10 enzymes (green), 8 ion channels (purple), 3 transporters (yellow) and 2 nuclear receptors (black). **f**, Dose-dependent inhibition curve of 5-HT_{2B} by HEP-50768. **g**, Effect of HEP-50768 on hERG channel activity assessed using a manual patch clamp. At 30 μM, HEP-50768 inhibited the hERG current by less than 20%. Cisapride, the positive control, exhibited an IC_{50} of 12.35 nM. **h**, HEP-50768 did not show mutagenic activity in the Ames test using *Salmonella* Typhimurium strains. The positive controls were as follows: TA97a: 9-AA (S9$^-$), 2-AA (S9$^+$); TA98: 2-NF (S9$^-$), 2-AA (S9$^+$); TA100: N4-ACT(S9$^-$), 2-AA (S9$^+$); TA102: 4-NQO (S9$^-$), 2-AA (S9$^+$); TA1535: N4-ACT (S9$^-$), 2-AA (S9$^+$) ($n = 30$ per group). All plots are representative of three biologically independent experiments, with each experimental data point collected with three technical replicates without statement. Data are shown as the mean ± s.e.m.

30 μM (Fig. 6g), suggesting a favorable cardiovascular safety margin at expected therapeutic exposures.

HEP-50768 does not exhibit mutagenic activity

The mutagenic potential of HEP-50768 was examined using the bacterial reverse mutation assay (Ames)[41] across five *Salmonella* Typhimurium strains (TA97a, TA98, TA100, TA102 and TA1535), with (S9$^+$) and without (S9$^-$) metabolic activation. All positive controls elicited clear mutagenic responses, while HEP-50768 induced no significant increase in revertant colonies at any tested concentration (Fig. 6h), indicating that HEP-50768 is nonmutagenic and lacks genotoxic potential.

The comprehensive in vitro safety profile indicates that HEP-50768 poses low risks of off-target effects, hERG-related cardiotoxicity or genotoxicity. Taken together with the favorable ADME and toxicity data from in vivo studies, HEP-50768 demonstrates a robust safety margin, supporting its continued development as a preclinical candidate targeting hX4.

Discussion

Chronic pruritus, particularly in cholestatic liver disease, remains debilitating and poorly treated, as it often resists antihistamines and corticosteroids. The discovery of hX4 as a bile-acid-responsive receptor has provided a mechanistic target for intervention. Here, we report HEP-50768, a potent and selective hX4 inverse agonist, and present a high-resolution cryo-EM structure of an inverse-agonist-bound hX4–G protein complex, revealing an intermediate GPCR–G protein conformation. HEP-50768 partially occupies the agonist-binding pocket, thereby blocking bile-acid-induced receptor activation and downstream itch signaling.

Functionally, HEP-50768 suppresses both basal and bile-acid-stimulated hX4 activity in vitro and dose-dependently reduces pruritogen-evoked scratching in hX4-humanized rats. The compound exhibits favorable PK, minimal off-target activity and negligible hERG inhibition, supporting a low risk of cardiac or serotonergic side effects. The 4-week toxicity studies revealed no hX4-related adverse effects, although long-term evaluation in humans, particularly with hepatic impairment, will be essential.

Overall, HEP-50768 demonstrates a compelling preclinical profile, combining mechanistic precision, efficacy and safety and represents a promising candidate for clinical development in cholestatic and potentially other forms of chronic itch. Investigational New Drug filing has been completed and phase I trials are planned, addressing an unmet need for targeted antipruritic therapy.

Online content

Any methods, additional references, Nature Portfolio reporting summaries, source data, extended data, supplementary information, acknowledgements, peer review information; details of author contributions and competing interests; and statements of data and code availability are available at https://doi.org/10.1038/s41589-026-02195-0.

References

1. Beuers, U., Wolters, F. & Oude Elferink, R. P. J. Mechanisms of pruritus in cholestasis: understanding and treating the itch. *Nat. Rev. Gastroenterol. Hepatol.* **20**, 26–36 (2023).
2. Vander Does, A., Levy, C. & Yosipovitch, G. Cholestatic itch: our current understanding of pathophysiology and treatments. *Am. J. Clin. Dermatol.* **23**, 647–659 (2022).
3. Combs, S. A., Teixeira, J. P. & Germain, M. J. Pruritus in kidney disease. *Semin. Nephrol.* **35**, 383–391 (2015).
4. Shirazian, S. et al. Chronic kidney disease-associated pruritus: impact on quality of life and current management challenges. *Int. J. Nephrol. Renov. Dis.* **10**, 11–26 (2017).
5. Steinhoff, M., Schmelz, M., Szabó, I. L. & Oaklander, A. L. Clinical presentation, management, and pathophysiology of neuropathic itch. *Lancet Neurol.* **17**, 709–720 (2018).
6. Yu, H. et al. Leveraging deep single-soma RNA sequencing to explore the neural basis of human somatosensation. *Nat. Neurosci.* **27**, 2326–2340 (2024).
7. Solinski, H. J., Gudermann, T. & Breit, A. Pharmacology and signaling of MAS-related G protein-coupled receptors. *Pharmacol. Rev.* **66**, 570–597 (2014).
8. Yu, H. et al. MRGPRX4 is a bile acid receptor for human cholestatic itch. *eLife* **8**, e48431 (2019).
9. Meixiong, J., Vasavda, C., Snyder, S. H. & Dong, X. MRGPRX4 is a G protein-coupled receptor activated by bile acids that may contribute to cholestatic pruritus. *Proc. Natl Acad. Sci. USA* **116**, 10525–10530 (2019).
10. Yu, H., Wangensteen, K., Deng, T., Li, Y. & Luo, W. MRGPRX4 in cholestatic pruritus. *Semin. Liver Dis.* **41**, 358–367 (2021).
11. Hegade, V. S. et al. Pruritus is common and undertreated in patients with primary biliary cholangitis in the United Kingdom. *Clin. Gastroenterol. Hepatol.* **17**, 1379–1387 (2019).
12. Piechota, J. & Jelski, W. Intrahepatic cholestasis in pregnancy: review of the literature. *J. Clin. Med.* **9**, 1361 (2020).
13. Yang, J. et al. Structure-guided discovery of bile acid derivatives for treating liver diseases without causing itch. *Cell* **187**, 7164–7182 (2024).
14. Chien, D. C.-C. et al. MRGPRX4 mediates phospho-drug-associated pruritus in a humanized mouse model. *Sci. Transl. Med.* **16**, eadk8198 (2024).
15. Yang, H., Chen, W., Zhu, R., Wang, J. & Meng, J. Critical players and therapeutic targets in chronic itch. *Int. J. Mol. Sci.* **23**, 9935 (2022).
16. Marenco-Flores, A. et al. Managing pruritus in chronic liver disease: an in-depth narrative review. *Clin. Liver Dis.* **23**, e0187 (2024).
17. Mayo, M. J. et al. A randomized, controlled, phase 2 study of maralixibat in the treatment of itching associated with primary biliary cholangitis. *Hepatol. Commun.* **3**, 365–381 (2019).
18. Hofmann, A. F. Rifampicin and treatment of cholestatic pruritus. *Gut* **51**, 756 (2002).
19. Hauser, A. S., Attwood, M. M., Rask-Andersen, M., Schiöth, H. B. & Gloriam, D. E. Trends in GPCR drug discovery: new agents, targets and indications. *Nat. Rev. Drug Discov.* **16**, 829–842 (2017).
20. Hauser, A. S. et al. Pharmacogenomics of GPCR drug targets. *Cell* **172**, 41–54 (2018).
21. Lorente, J. S. et al. GPCR drug discovery: new agents, targets and indications. *Nat. Rev. Drug Discov.* **24**, 458–479 (2025).
22. Clapham, D. E. Calcium signaling. *Cell* **80**, 259–268 (1995).
23. Schroeder, K. S. & Neagle, B. D. FLIPR: a new instrument for accurate, high throughput optical screening. *J. Biomol. Screen.* **1**, 75–80 (1996).
24. Cao, C. et al. Structure, function and pharmacology of human itch GPCRs. *Nature* **600**, 170–175 (2021).
25. Ma, Q., Lingyan, Y., Hongxia, L., Ying, S. & Zhou, N. An overview of Ca^{2+} mobilization assays in GPCR drug discovery. *Expert Opin. Drug Discov.* **12**, 511–523 (2017).
26. Vetter, I. et al. in *Calcium Signaling* (ed. Islam, M. S.) Ch. 3 (Springer, 2020).
27. Shen, R. R., Lei, X., Wang, X., Li, Y. & He, R. Compounds, compositions and methods thereof. WIPO patent WO2024/083210 (2024).
28. A. Yeager et al. Modulators of MAS-related G-protein receptor X4 and related products and methods. US patent US20230053860 (2023).
29. Zhang, K., Wu, H., Hoppe, N., Manglik, A. & Cheng, Y. Fusion protein strategies for cryo-EM study of G protein-coupled receptors. *Nat. Commun.* **13**, 4366 (2022).
30. Robertson, M. J. et al. Structure determination of inactive-state GPCRs with a universal nanobody. *Nat. Struct. Mol. Biol.* **29**, 1188–1195 (2022).
31. Tyson, A. S. et al. Molecular mechanisms of inverse agonism via κ-opioid receptor–G protein complexes. *Nat. Chem. Biol.* **21**, 1046–1057 (2025).
32. Kim, K. et al. Structure of a hallucinogen-activated G_q-coupled 5-HT_{2A} serotonin receptor. *Cell* **182**, 1574–1588 (2020).
33. Zhou, Q. et al. Common activation mechanism of class A GPCRs. *eLife* **8**, e50279 (2019).
34. White, K. L. et al. Structural connection between activation microswitch and allosteric sodium site in GPCR signaling. *Structure* **26**, 259–269 (2018).
35. Guo, Q. et al. A method for structure determination of GPCRs in various states. *Nat. Chem. Biol.* **20**, 74–82 (2024).
36. Zhang, Y. et al. Single-particle cryo-EM structural studies of the β_2AR–G_s complex bound with a full agonist formoterol. *Cell Discov.* **6**, 45 (2020).
37. Zhang, H. et al. Structure of the angiotensin receptor revealed by serial femtosecond crystallography. *Cell* **161**, 833–844 (2015).
38. Redfern, W. S. et al. Relationships between preclinical cardiac electrophysiology, clinical QT interval prolongation and torsade de pointes for a broad range of drugs: evidence for a provisional safety margin in drug development. *Cardiovasc. Res.* **58**, 32–45 (2003).
39. Leishman, D. J., Abernathy, M. M. & Wang, E. B. Revisiting the hERG safety margin after 20 years of routine hERG screening. *J. Pharmacol. Toxicol. Methods* **105**, 106900 (2020).

40. Harmer, A. R. & Rolf, M. G. On the relationship between hERG inhibition and the magnitude of QTc prolongation: an in vitro to clinical translational analysis. *Toxicol. Appl. Pharmacol.* **492**, 117135 (2024).
41. Mortelmans, K. & Zeiger, E. The Ames *Salmonella*/microsome mutagenicity assay. *Mutat. Res.* **455**, 29–60 (2000).

Publisher's note Springer Nature remains neutral with regard to jurisdictional claims in published maps and institutional affiliations.

Springer Nature or its licensor (e.g. a society or other partner) holds exclusive rights to this article under a publishing agreement with the author(s) or other rightsholder(s); author self-archiving of the accepted manuscript version of this article is solely governed by the terms of such publishing agreement and applicable law.

© The Author(s), under exclusive licence to Springer Nature America, Inc. 2026

Methods

General

Primers were synthesized at Xianghong. DNA sequencing was performed by RuiBiotech. The ClonExpress II one-step cloning kit was purchased from Vazyme Biotech. PCR was performed to generate DNA fragments using standard thermal cycling protocols with TransStart FastPfu DNA polymerase (Transgene Biotech). The PK and toxicokinetic studies in SD rats and rhesus monkeys were conducted in JOINN Laboratories. HEK293T cell lines stably expressing hX4 were constructed in a previous study[8] and HEK293T cell lines stably expressing the hERG channel was purchased from SARL Creacell. SD rats were purchased from Zhejiang Vital River Laboratory Animal Technology. Male rats (7–8 weeks old, 236–278 g) and female rats (7–8 weeks old, 218–250 g) were used for all animal experiments. All animals were group-housed (3–5 animals per cage) under a standard 12-h light–dark cycle and all behavioral experiments were performed during the light cycle. Rhesus monkeys were purchased from Yunnan Yinmore Biotech. Male monkeys (2.5–8 years old, 5.10–9.28 kg) and female monkeys (2.5–8 years old, 2.96–5.32 kg) were used for all animal experiments. All animal experiments were approved by the Animal Care and Use Committee of Peking University of Life Sciences.

Construction

For protein expression of hX4 in sf9 insect cells, the gene for the S83 variant of hX4 was cloned into a modified pFastBac1 vector, which contains a hemagglutinin (HA) signal peptide followed by a Flag tag, His_{10} tag, a tobacco etch virus protease site, a thermostabilized apocytochrome b562RIL (BRIL) and an HRV3C protease at the N terminus of the receptor. For G_q and scFv16 protein, we used the same mini$G\alpha_q$iN heterotrimer and scFv16 as reported in the earlier hX4 structural study[24]. For the calcium mobilization assay of mutants, the genes of wild-type hX4 or its variants were cloned into a pcDNA3.1-NFlag vector.

High-throughput screening of hX4 antagonists

A fluorescence-based calcium mobilization assay was used to screen for hX4 antagonists. Cells stably expressing hX4 were cultured in plating medium (DMEM containing 1% (v/v) FBS and 1% penicillin–streptomycin) and then were plated into poly(L-lysine)-coated 384-well black clear-bottom cell culture plates in plating medium at a density of 17,000 cells in 20 µl per well and incubated overnight at 37 °C, 5% CO_2. After approximately 18 h, the plate medium was discarded and 20 µl of dye loading buffer (Hanks' balanced salt solution (HBSS) buffer containing 2 µM Fluo-8, pH 7.4) was loaded into each well and incubated at room temperature for 1 h. Then, 10 µl of 3× compound dissolved in HBSS buffer (pH 7.4) was transferred to the cell plate per well by FLIPR and then incubated at room temperature for 30 min. After that, 10 µl of 6× stimulation buffer (containing 60 µM DCA) was transferred to each well of the cell plate using FLIPR, followed by continued fluorescence measurement for 120 s. Data were normalized to the rate of inhibition of compounds to DCA-induced calcium mobilization. The library screened in this study comprised approximately 100,000 compounds, including 5,000 natural products, 3,500 drugs approved by the US Food and Drug Administration and about 91,500 drug-like small molecules.

Dose-dependent inhibition of antagonists to hX4

Cells stably expressing hX4 were cultured in DMEM containing 10% FBS, 100 U per ml penicillin–streptomycin, 20 mM HEPES and 1 µg ml^{-1} puromycin, plated into poly(D-lysine)-coated 384-well black clear-bottom plates at a density of 15,000 cells with 20 µl per well and incubated overnight at 37 °C, 5% CO_2. Subsequently, the plate medium was discarded and 20 µl of HBSS buffer (containing 2 µM Fluo-8) was added to each well, followed by incubation at room temperature for 1 h. Then, 10 µl of 3× compound at various concentrations was transferred to the cell plate and incubated at room temperature for 30 min. Subsequently, 10 µl of 6× stimulation buffer was added to the cell plate and fluorescence was measured for an additional 120 s.

GTPase-Glo assay

The GTPase activity of purified hX4 was assessed using the GTPase-Glo assay system. Purified hX4 was diluted to concentrations of 0.5, 1, 2 and 3 µM in a reaction buffer containing 20 mM HEPES pH 7.4, 100 mM NaCl, 0.01% lauryl maltose neopentyl glycol (LMNG), 0.001% cholesteryl hemisuccinate (CHS) and 20 µM GTP. Each receptor dilution was supplemented with either 2 µM DCA-3P or 2 µM HEP-50768 and incubated at room temperature for 1.5 h. Concurrently, G_q protein purified by DDM was subjected to detergent exchange by incubation with 1% LMNG and 0.1% CHS on ice for 1 h. The detergent-exchanged G_q was then diluted to 1 µM in a solution containing 20 mM HEPES pH 7.4, 100 mM NaCl, 0.01% LMNG, 0.001% CHS, 20 µM GDP, 200 µM TCEP and 20 mM $MgCl_2$. Equal volumes of the receptor and G_q solutions were combined and incubated at room temperature for 60 min with gentle shaking. Subsequently, an equal volume of GTPase-Glo reagent supplemented with 10 µM ADP in the same detergent-containing buffer was added to the mixture, which was then incubated with gentle shaking for 30 min. An equal volume of detection reagent was then introduced and, after an additional 10-min incubation, luminescence intensity was measured using an Envision plate reader. Control experiments were conducted to determine baseline GTP levels by mixing equal volumes of receptor and G_q buffers. Inherent G protein turnover was assessed by combining the G_q solution with receptor buffer in the absence of hX4.

Expression and purification of HEP-50768 bound hX4

For the expression of hX4–G_q–scFv16 complex, sf9 cells at a density of 2×10^6 cells per ml were coinfected with hX4, mini$G\alpha_q$iN heterotrimer and scFv16 viruses generated by a Bac-to-Bac Baculovirus expression system (Invitrogen) at a 2:1:1 multiplicity of infection. After 48 h, the cells were harvested and stored at −80 °C until further use. On the day of purification, the hX4–G_q-expressing cells were thawed on ice and homogenized in a buffer containing 20 mM HEPES, 50 mM NaCl, 1 mM $MgCl_2$ and a proteinase inhibitor at room temperature. Following a 1-h incubation, the cell membranes were collected by centrifugation at 25,000*g* for 30 min using a Beckman Ti45 rotor. The cell membranes were then solubilized in a buffer containing 20 mM HEPES, 100 mM NaCl, 5% (w/v) glycerol, 0.6% (w/v) LMNG, and 0.06% (w/v) CHS for 3 h at 4 °C. After centrifugation at 32,000*g* for 30 min using a Ti70 rotor (Beckman), the supernatant was transferred to a 50-ml conical tube and incubated overnight at 4 °C with 0.8 ml of Talon resin (Takara) and 20 mM imidazole. The following day, the resin was collected and washed with 20 ml of washing buffer containing 20 mM HEPES, 100 mM NaCl, 5% (w/v) glycerol, 0.01% (w/v) LMNG, 0.001% (w/v) CHS and 30 mM imidazole. The hX4–G_q–scFv16 complex protein was subsequently eluted using a buffer containing 20 mM HEPES, 100 mM NaCl, 5% (w/v) glycerol, 0.01% (w/v) LMNG, 0.001% (w/v) CHS and 250 mM imidazole. The eluted protein was concentrated and purified by size-exclusion chromatography on a Superdex 200 Increase 10/300 column (GE Healthcare), preequilibrated with a buffer containing 20 mM HEPES pH 7.5, 100 mM NaCl, 0.00075% (w/v) LMNG, 0.00025% (w/v) glyco-diosgenin, 0.00075% (w/v) CHS and 100 µM TCEP. A single fraction corresponding to the peak was concentrated to 3–5 mg ml^{-1} and incubated with 100 µM HEP-50768 for 2 h before being prepared for grid analysis.

Cryo-EM grid preparation, data collection and processing

First, 3.0 µl of protein samples were applied to glow-discharged Quantifoil R1.2/1.3 Au 300-mesh holey carbon grids individually and flash-frozen in liquid ethane using a Vitrobot Mark IV (FEI) set at 4 °C and 100% humidity, with a blot time of 4–5 s. The grids were subsequently loaded into a 300-kV Titan Krios microscope equipped with an energy filter and a K3 direct electron detector (Gatan). Data collection was performed automatically using EPU software in counting mode, with a physical pixel size of 0.82 Å and a defocus range of −1.0 to −1.8 µm. Each image stack was fractionated into 40 frames with a total

accumulated dose of 50 electrons per Å^2. The collected movies were then imported to cryoSPARC for patch motion correction and patch contrast transfer function estimation[42]. The curated images were then subjected to blob picking. Following several rounds of two-dimensional and three-dimensional classification, the best three-dimensional class was then subjected to homogeneous refinement and nonuniform refinement[43]. A local refinement focused on the receptor region was further performed to yield a more precise receptor map. The map resolutions at a Fourier shell correlation of 0.143 (ref. 44) are reported in Supplementary Table 2.

Model building and refinement

Structural models of hX4, the miniG_q heterotrimer and scFv16, derived from the fospropofol-bound hX4–G_q–scFv16 complex (PDB 8YRG)[14], were rigid-body docked into the cryo-EM density map of HEP-50768-bound hX4–G_q–scFv16 complex or HEP-50768-bound hX4 receptor-only map using ChimeraX (version 1.2.5)[45]. The initial model was then subjected to iterative manual refinement in Coot (version 0.9.4)[46], followed by multiple cycles of real-space refinement in PHENIX (version 1.18.2)[47] to obtain the final model. Model validation was performed with MolProbity[48]. Structural figures were prepared using ChimeraX (version 1.2.5) or PyMOL (version 3.0.4). The refinement statistics are available in Supplementary Table 2.

Activity assessment of HEP-50768 toward hX4 mutants using FLIPR assay

HEK293T cells were maintained in DMEM supplemented with 10% FBS and 1% penicillin–streptomycin at 37 °C in a humidified incubator with 5% CO_2. For transfection, cells were seeded into six-well plates at a density of 1×10^6 cells per well. After 16–18 h, cells were transfected with 4 µg of plasmid DNA encoding either wild-type hX4 or its mutant variants, all of which were cloned into the pcDNA3.1-NFlag expression vector. Transfections were performed using polyethylenimine (PEI) at a DNA:PEI mass ratio of 1:5 in Opti-MEM (Thermo Fisher Scientific), following the manufacturer's instructions. Approximately 24 h after transfection, cells were detached with 0.05% trypsin–EDTA and seeded into poly(D-lysine)-coated, black clear-bottom 96-well plates (Corning) at a density of 5×10^4 cells per well in complete medium. Cells were incubated overnight under standard culture conditions (37 °C, 5% CO_2). The next day, intracellular calcium inhibition responses to HEP-50768 were measured using the Fluo-8 no-wash calcium assay kit (AAT Bioquest), following the manufacturer's protocol as previously described. Briefly, cells were loaded with Fluo-8 dye for 1 h at room temperature, followed by treatment with HEP-50768 at different concentration. Calcium mobilization was then induced using DCA at a concentration corresponding to the EC_{80} for each hX4 variant. Fluorescence was recorded using the FLIPR Tetra system. The inhibitory effect of HEP-50768 on each hX4 mutant was quantified relative to vehicle control and normalized to the maximum activity of the corresponding variant. All assays were performed in triplicate unless otherwise stated.

MD simulations

MD simulations were conducted according to the previous reported method with hX4 and ligands without G protein[13]. CHARMM-GUI[49] was used to generate the system, POPC was used to build the phospholipid bilayer and the concentration of NaCl was set to 0.15 M. The ff14SB force field, the gaff force field, the TIP3P model and the lipid14 force field parameters were used for protein, ligands, water and lipids, respectively, with the Leap module of the AmberTools21. Three independent 100-ns MD simulations were performed for each complex structure. The analysis of the trajectory was performed in Chimera (version 1.15).

Expression level analysis of hX4 mutants in HEK293T cells

Cells were transfected with 4 µg of plasmid DNA encoding either wild-type hX4 or its mutant variants, all of which were cloned into the pcDNA3.1-NFlag expression vector. Transfection was performed using PEI at a DNA:PEI mass ratio of 1:5 in Opti-MEM (Thermo Fisher Scientific). Approximately 48 h after transfection, the cells were harvested by detaching with 0.05% trypsin–EDTA, washed with PBS and then lysed in RIPA buffer supplemented with protease inhibitors. Equal amounts of total protein were subjected to SDS–PAGE and then transferred to PVDF membranes. Western blotting was performed using anti-Flag M2 antibody (Abclonal) to detect hX4 expression. The relative expression levels of hX4 and its variants were quantified by densitometric analysis using ImageJ software[50].

Scratching behavioral studies in hX4-humanized rats

To evaluate the antipruritic efficacy of HEP-50768, scratching behavior was assessed in hX4-humanized rats following DCA-3S-induced itch. Adult rats were housed under standard laboratory conditions and acclimated to individual recording chambers for 30 min per day for three consecutive days before behavioral testing to minimize stress-induced variability. On the day of the experiment, animals were randomly assigned to treatment groups. Specifically, 5 or 10 mg kg^{-1} HEP-50768 or PBS (as vehicle) was administered through oral gavage 2.5 h before pruritogen injection. Scratching behavior was recorded for 1 h using a high-definition video camera before 50 µg in 50 µl of DCA-3S was injected intradermally into the nape of the neck. Immediately after pruritogen injection, rats were placed in the recording chambers and spontaneous scratching behavior was recorded for 1 h. A scratch was defined as lifting the hind paw to the neck region, followed by a series of rapid scratching movements and then returning the paw to the floor. The number of scratching bouts was manually counted by trained observers blinded to the treatment conditions.

PK study of HEP-50768 in SD rats

A total of 30 SD rats (15 males and 15 females) were randomly assigned to five groups with six animals in each group (three males and three females) to evaluate the PK profile of HEP-50768 following different dosing regimens. Groups 1–3 received a single oral dose of HEP-50768 at 5, 15 or 50 mg kg^{-1}, respectively. Blood samples were collected at the following time points: before dose and 0.25 h, 0.5 h, 1 h, 4 h, 8 h, 12 h, 24 h, 36 h, 48 h, 60 h and 72 h after dose. Group 4 received a single i.v. at dose of 5 mg kg^{-1}. Blood samples were collected at the following time points: before dose and 5 min, 0.25 h, 0.5 h, 1 h, 2 h, 4 h, 6 h, 8 h, 12 h, 24 h and 48 h after dose. Group 5 received once-daily oral administration of HEP-50768 at 15 mg kg^{-1} for seven consecutive days. On day 7, serial blood samples were collected at the following time points: before dose and 5 min, 0.25 h, 0.5 h, 1 h, 4 h, 8 h, 12 h, 24 h, 36 h, 48 h, 60 h, 72 h and 96 h after the final dose. Plasma was isolated by centrifugation and stored at −80 °C until analysis. HEP-50768 concentrations in plasma were quantified using a validated liquid chromatography–tandem mass spectrometry (LC–MS/MS) method. PK parameters were calculated using WinNonlin software (version 8.3.5.340; Certara) by noncompartmental analysis (NCA).

PK study of HEP-50768 in rhesus monkeys

A total of 12 rhesus monkeys (six animals per sex) were randomly assigned to two groups: the continuous-dose group and the single-dose group, with three animals per sex in each group. Animals in the continuous-dose group were administered HEP-50768 at a dose of 7.5 mg kg^{-1} through oral gavage once daily for seven consecutive days. Animals in the single-dose group were administered a single dose of 2.5 mg kg^{-1} HEP-50768 through i.v. bolus. Following this dosing, the animals were subsequently assigned to the low-dose, middle-dose and high-dose groups in sequence, receiving single oral doses of 2.5, 7.5 and 25 mg kg^{-1} HEP-50768, respectively. The blood samples were collected at the following time points: continuous-dose group before dose and 0.25, 0.5, 1, 2, 4, 6, 8, 12 and 24 h after dose on day 1 and day 7; i.v. group before dose and 5 min, 0.25, 0.5, 1, 2, 4, 6, 8, 12, 24, 36 and 48 h

after dose; other oral groups before dose and 0.25, 0.5, 1, 2, 4, 6, 8, 12, 24, 36, 48, 72 and 96 h after dose. The concentrations of HEP-50768 in monkey plasma samples were determined using a validated LC–MS/MS method. PK parameters were calculated using NCA through WinNonlin software (version 8.3.5.340; Certara) to assess the PK characteristics of HEP-50768 in monkeys.

Tissue distribution of HEP-50768 in SD rats

A total of 24 SD rats (12 males and 12 females) were randomly assigned to 4 groups ($n = 6$; three males and three females). Animals were administered a single dose of HEP-50768 at 5 mg kg^{-1} through oral gavage. Blood and tissue samples were collected from the animals in each group at 0.5, 6, 12 and 24 h after dose. The collected tissues were as follows: skin, brain, heart, liver, spleen, lung, kidney, stomach (without contents), small intestine, large intestine, muscle, fat, bone marrow, spinal cord and gonad (male: testis, female: ovary). The concentrations of HEP-50768 in rat plasma and tissue homogenate samples were determined using validated LC–MS/MS methods. PK parameters were calculated using NCA through WinNonlin software (version 8.3.5.340; Certara) to assess the distribution characteristics of HEP-50768 in rats.

Excretion study of HEP-50768 after oral gavage in SD rats

A total of 16 SD rats (eight males and eight females) were randomly assigned to two groups: the feces and urine group (normal rats, three animals per gender) and the bile group (bile-duct-cannulated model rats, five animals per gender). The animals received a single oral gavage dose of HEP-50768 at a dose of 5 mg kg^{-1}. Bile samples were collected from the bile group at the following time intervals after administration: 0–4 h, 4–8 h, 8–24 h, 24–32 h, 32–48 h, 48–56 h, 56–72 h and 72–96 h. Among them, six animals (three per gender) were selected for sample analysis. Feces and urine samples were collected from the feces and urine group at the following time intervals after administration: 0–4 h, 4–8 h, 8–24 h, 24–32 h, 32–48 h, 48–56 h, 56–72 h, 72–80 h, 80–96 h, 96–104 h, 104–120 h, 120–128 h, 128–144 h, 144–152 h and 152–168 h. The concentrations of HEP-50768 in the feces supernatant, urine and bile were analyzed using a validated LC–MS/MS method. The excretion, excretion rate and cumulative excretion rate of the parental drug HEP-50768 in bile, feces and urine in each period were calculated on the basis of the obtained concentrations.

Toxicity study of HEP-50768 by oral gavage to SD rats

A total of 120 SD rats (60 male and 60 female) were randomly assigned to four groups. Animals in group 1 were treated with purified water as the vehicle control. Animals in groups 2–4 were treated with HEP-50768 at doses of 6, 20 and 60 or 50 mg kg^{-1} as the low-dose, middle-dose and high-dose groups, respectively. An obvious toxicity response (death) was noted in animals of group 4 that were treated with HEP-50768 at dose of 60 mg kg^{-1} from day 1 to day 7, discontinued for 7 days from day 8 to day 14 and then given a reduced dose of 50 mg kg^{-1} from day 15 to day 28. Animals were administered through oral gavage with a volume of 10 ml kg^{-1} once daily for 28 days (21 days for the high-dose groups). Plasma was isolated by centrifugation and stored at −80 °C until analysis. HEP-50768 concentrations in plasma were quantified using a validated LC–MS/MS method. PK parameters were calculated using NCA through WinNonlin software (version 8.3.5.340; Certara).

Toxicity study of HEP-50768 by oral gavage to rhesus monkeys

A total of 40 healthy rhesus monkeys (20 males and 20 females) were enrolled in a 28-day repeated-dose oral toxicokinetic study. Animals were stratified by sex and randomly assigned into four treatment groups ($n = 5$ per sex per group). Group 1 received purified water and served as the vehicle control. Groups 2, 3 and 4 received HEP-50768 at doses of 5, 25 and 120 or 60 mg kg^{-1} daily, respectively. For group 4, male monkeys received 120 mg kg^{-1} from day 1 to day 6 and 60 mg kg^{-1} from day 7 to day 28. Female monkeys received 60 mg kg^{-1} of the compound throughout the 28-day dosing period. All animals were administered a single dose of the test substance through oral gavage once daily for 28 consecutive days at a dose volume of 5 ml kg^{-1}. For toxicokinetic analysis, plasma samples were collected on day 1 and day 28 for all dose groups, as well as on day 8 for male monkeys in the high-dose group (60 mg kg^{-1}). Plasma concentrations of HEP-50768 were quantified using a validated LC–MS/MS method. Toxicokinetic parameters were calculated using NCA through WinNonlin software (version 8.3.5.340; Certara).

Manual patch-clamp technology to determine hERG inhibition of HEP-50768

The HEK293 cells stably expressing the hERG channel were cultured in DMEM supplemented with 10% FBS and 0.8 mg ml^{-1} G418 in a culture dish. Cells were grown in a humidified incubator at 37 °C with 5% CO_2. Before the patch-clamp test, the cells were detached using TrypLE Express solution. Then, 4×10^3 cells were seeded into a 24-well plate (final medium volume: 500 µl) with one coverslip in each well and tested after 18 h. The hERG current was recorded using the whole-cell patch-clamp technique at a holding potential of −80 mV and then depolarized to −50 mV for 0.5 s to test the leak current. Then, the voltage was depolarized to 30 mV for 2.5 s. The peak tail current was induced by a repolarizing pulse to −50 mV for 4 s. This protocol was repeated at 10-s intervals to observe the effect of the test article on hERG tail current. The data were collected using an IPA amplifier (Sutter Instrument) and stored in SutterPatch (with Igor Pro) software. The patch clamp was operated by pulling the glass pipette first using a micropipette puller. Then, the micropipette filled with intracellular solution was loaded into the pipette holder and was manipulated using a micromanipulator under an inverted microscope. The pipette was lowered into the recording solution and the resistance (R_{pip}) was noted. After touching the cell, a slight suction was applied to achieve a high resistance seal (in the GΩ range). Fast capacitance compensation was performed and negative pressure was continued to break the membrane into whole-cell mode. Then, the slow capacitance was compensated and experimental parameters such as series resistance (R_s) were recorded. No leak subtraction was made. Cells were incubated with the test article for about 5 min or until the current reached a steady-state level. Multiple concentrations of the test article were tested. A coverslip lined with cells was placed in a recording chamber under an inverted microscope. The control and test solutions flew sequentially through the chamber from low to high concentration through a gravity-fed solution delivery system. During the experiment, the solutions were withdrawn from the chamber by a peristaltic pump. The current of each cell detected in the extracellular solution without the compound was used as its blank control. The assay was repeated three times independently using at least three cells per concentration. All tests were performed at room temperature.

Mutagenicity test of HEP-50768 in *Salmonella* Typhimurium

The mutagenicity of HEP-50768 was evaluated using histidine-deficient *Salmonella* Typhimurium test strains TA97a, TA98, TA100, TA102 and TA1535. The vehicle control group (sterile water for injection), test article groups (500, 150, 75, 20 and 10 µg per plate selected as the five doses of HEP-50768 for TA97a and TA98 strains; 150, 75, 50, 20 and 10 µg per plate selected as the five dose of HEP-50768 for TA100, TA1535 and TA98 strains; 1,500, 500, 150, 75 and 20 µg per plate selected as the five dose of HEP-50768 for TA102 strain) and positive control groups (direct mutagens 9-aminoacridine, 2-nitrofluorene, N^4-aminocytidine and 4-nitroquinoline *N*-oxide and indirect mutagen 2-aminoanthracene) were included. Additionally, to further evaluate the effect of metabolites, HEP-50768 was incubated with SD rat liver (S9). After incubation for about 65.5 h at 37 °C with metabolic activation (S9 mix added, +S9) or without metabolic activation (PBS added, −S9), revertant colonies were counted on all plates. Each treatment consisted of triplicate plates.

Quantification and statistical analysis

Statistical analyses were performed using GraphPad Prism 9.0. Group data were analyzed using unpaired *t*-tests and Mann–Whitney tests (*$P < 0.05$ and **$P < 0.01$; NS, not significant: $P > 0.05$).

Chemical synthesis of HEP-50768

HEP-50768 was synthesized using chemical strategies. The synthetic route is shown in the Supplementary Protocols.

Reporting summary

Further information on research design is available in the Nature Portfolio Reporting Summary linked to this article.

Data availability

Cryo-EM data of the HEP-50768-bound hX4–G_q complex were deposited to the Protein Data Bank and EM Data Bank under accession codes PDB 9V81 and EMD-64829, respectively, and are publicly available as of the date of publication. Cryo-EM data of local refined structure of HEP-50768-bound hX4 were deposited to the Protein Data Bank and EM Data Bank under accession codes PDB 9V82 and EMD-64830, respectively, and are publicly available as of the date of publication. The MD simulation input files and trajectories were deposited to Zenodo (https://doi.org/10.5281/zenodo.18778909)[51]. Source data are provided with this paper.

References

42. Punjani, A., Rubinstein, J. L., Fleet, D. J. & Brubaker, M. A. cryoSPARC: algorithms for rapid unsupervised cryo-EM structure determination. *Nat. Methods* **14**, 290–296 (2017).
43. Punjani, A., Zhang, H. & Fleet, D. J. Non-uniform refinement: adaptive regularization improves single-particle cryo-EM reconstruction. *Nat. Methods* **17**, 1214–1221 (2020).
44. Rosenthal, P. B. & Henderson, R. Optimal determination of particle orientation, absolute hand, and contrast loss in single-particle electron cryomicroscopy. *J. Mol. Biol.* **333**, 721–745 (2003).
45. Pettersen, E. F. et al. UCSF Chimera—a visualization system for exploratory research and analysis. *J. Comput. Chem.* **25**, 1605–1612 (2004).
46. Emsley, P. & Cowtan, K. Coot: model-building tools for molecular graphics. *Acta Crystallogr. D* **60**, 2126–2132 (2004).
47. Adams, P. D. et al. PHENIX: a comprehensive Python-based system for macromolecular structure solution. *Acta Crystallogr. D* **66**, 213–221 (2010).
48. Chen, V. B. et al. MolProbity: all-atom structure validation for macromolecular crystallography. *Acta Crystallogr. D* **66**, 12–21 (2010).
49. Kern, N. R., Lee, J., Choi, Y. K. & Im, W. CHARMM-GUI Multicomponent Assembler for modeling and simulation of complex multicomponent systems. *Nat. Commun.* **15**, 5459 (2024).
50. Schneider, C. A., Rasband, W. S. & Eliceiri, K. W. NIH Image to ImageJ: 25 years of image analysis. *Nat. Methods* **9**, 671–675 (2012).
51. Yang, J. MD simulation files. *Zenodo* https://doi.org/10.5281/zenodo.18778909 (2026).

Acknowledgements

We thank Y. Rao (Peking University) for support with the FLIPR device. We thank the Cryo-EM Center of the University of Science and Technology of China for use of the EM facility. We are grateful to Y. Gao and all other staff members at the Cryo-EM Center for technical support during cryo-EM data collection. This work was funded by grants from the National Key Research and Development Program of China (2022YFC2502500 and 2022YFC3401500 to X.L.), National Natural Science Foundation of China (22337002, 92253305 and 22193073 to X.L.; GG9100007022 to C.C.; 82504820 to C.W.), Center for Advanced Interdisciplinary Science and Biomedicine of IHM (2023KYQD012 to C.C.), Beijing National Laboratory for Molecular Sciences (BNLMS-CXXM-202106 to X.L.), the Chinese Institutes for Medical Research, Beijing (CX23YZ18 to X.L.), New Cornerstone Science Foundation through the New Cornerstone Investigator Program and the XPLORER prize (to X.L.), and the startup funding of University of Science and Technology of China (KY9100000088 to C.C.). J.Y. is supported by the Boya Postdoctoral Fellowship of Peking University, and the Postdoctoral Fellowship Program and a China Postdoctoral Science Foundation (BX20250151).

Author contributions

X.L. initiated and managed the whole project. R.S. and X.W. designed the high-throughput screening of hX4 antagonists with the help of Y. Li. C.W. determined the cryo-EM structure of hX4 bound to HEP-50768 under the guidance of C.C. J.Y. performed the MD simulations with assistance from H.K. and conducted the functional assay with the help of W.Z., J.F., M.Z. and G.L. R.S. and Y. Liu designed the ADME experiments and J.Y. analyzed the results. S.L. and X.W. synthesized the compounds used in this work. J.Y., X.L., R.S., C.W. and C.C. wrote the paper with input from all authors.

Competing interests

Two patents related to this work, WO 2024/083210 and WO 2024/174995, were filed by Hepai Tech, with R.S., X.L., Y. Li and X.W. as coinventors. The other authors declare no competing interests.

Additional information

Extended data is available for this paper at https://doi.org/10.1038/s41589-026-02195-0.

Supplementary information The online version contains supplementary material available at https://doi.org/10.1038/s41589-026-02195-0.

Correspondence and requests for materials should be addressed to Can Cao or Xiaoguang Lei.

Peer review information *Nature Chemical Biology* thanks Jianjun Cheng and the other, anonymous reviewers for their contribution to the peer review of this work.

Reprints and permissions information is available at www.nature.com/reprints.

https://doi.org/10.1038/s41589-026-02195-0

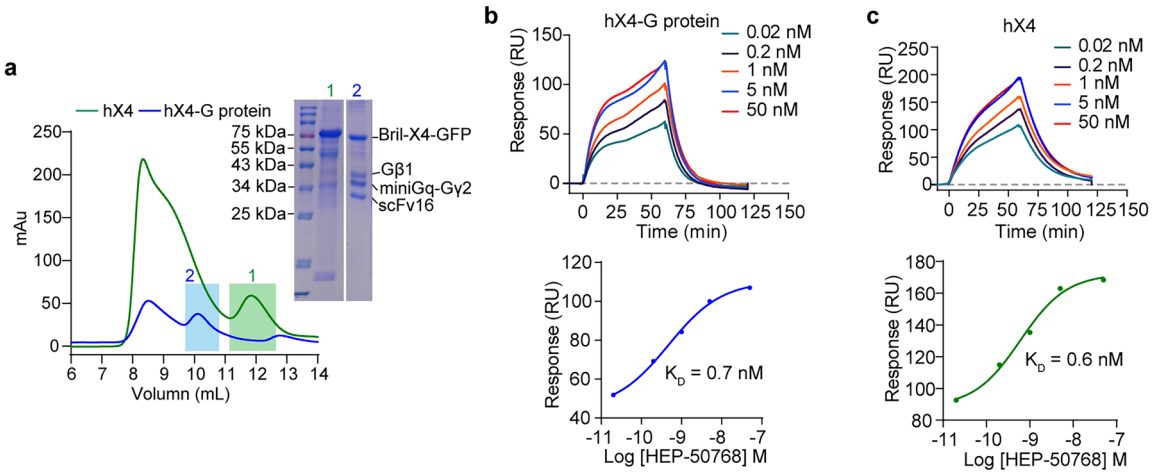

Extended Data Fig. 1 | Affinity of HEP-50768 to hX4 in the absence or presence of G protein. a, Purification of hX4 in the absence and presence of G protein. This experiment was repeated three times independently. **b-c**, Surface plasmon resonance (SPR) analysis of HEP-50768 binding to hX4 in the presence (**b**) and absence (**c**) of G protein. Comparable affinities were observed in both conditions. Top panel: Response-Time curve; Bottom panel: Response-Concentration curve. All plots are representative of three biologically independent experiments, with each experimental data point collected with three technical replicates.

https://doi.org/10.1038/s41589-026-02195-0

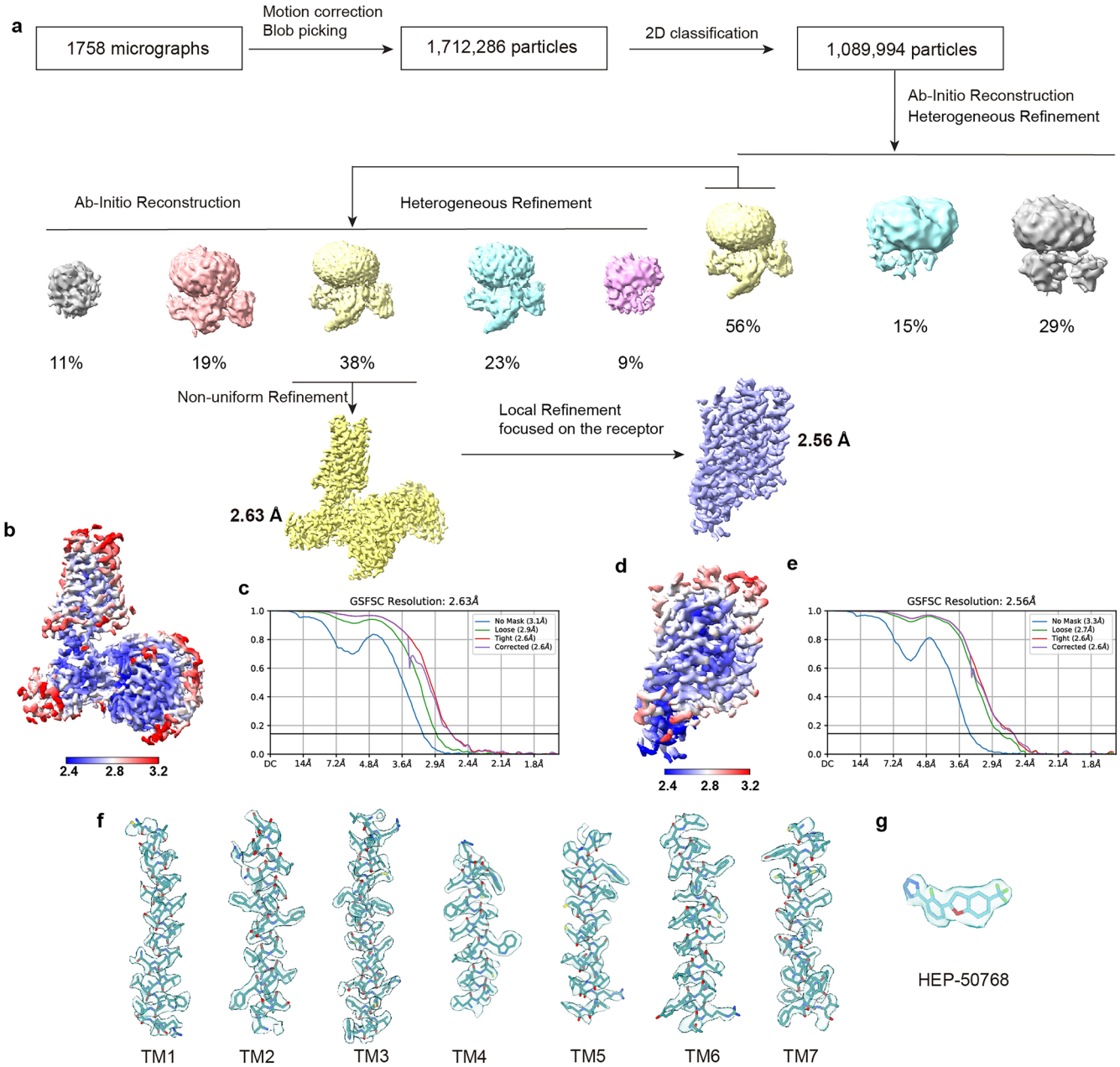

Extended Data Fig. 2 | Structural determination of HEP-50768-bound hX4-Gq-sFv16 complex and the cryo-EM density map. a, Cryo-EM data processing flow chart of HEP-50768-bound hX4-Gq-scFv16 complex. **b-c**, Local resolution **(b)** and the Fourier shell correlation (FSC) curves **(c)** of HEP-50768-bound hX4-Gq-scFv16 complex. **(d-e)** Local resolution **(d)** and the FSC curves **(e)** of the local refinement map of HEP-50768-bound hX4. **f-g**, the cryo-EM density map of TM1-TM7 **(f)** and HEP-50768 **(g)** in the local refinement map of HEP-50768-bound hX4.

https://doi.org/10.1038/s41589-026-02195-0

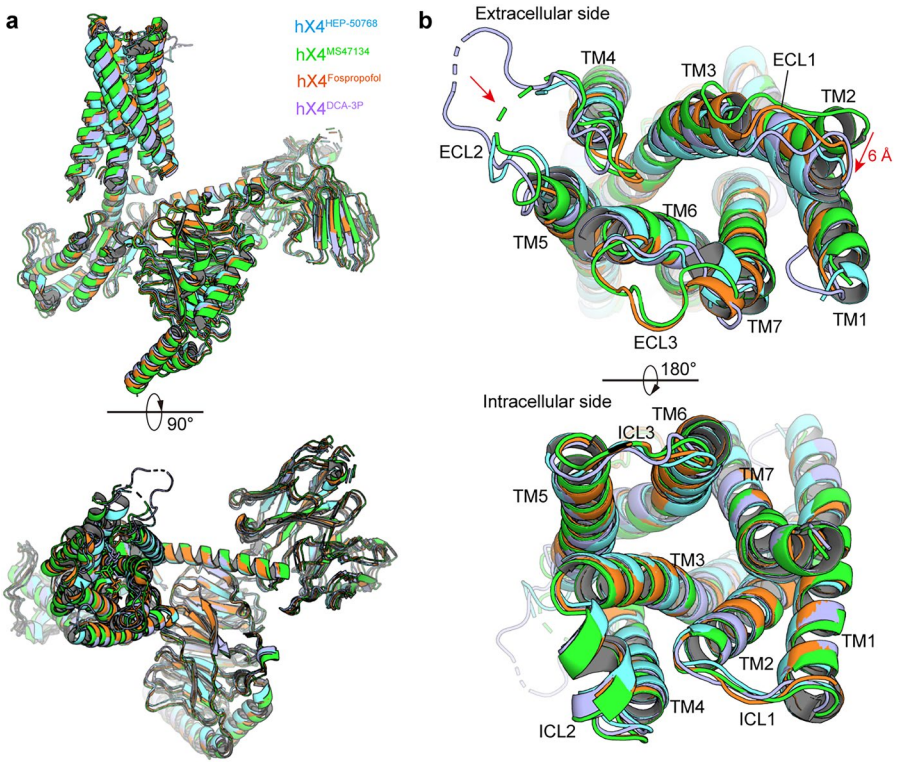

Extended Data Fig. 3 | Overall structural alignment of HEP-50768-bound hX4-Gq-scFv16 complex with agonist-bound structures. a, Structural comparison of HEP-50768-bound hX4-G protein complex ($hX4^{HEP\text{-}50768}$, cyan) with agonists-bound hX4 structures: MS47134 ($hX4^{MS47134}$, green), Fospropofol ($hX4^{Fospropofol}$, orange) and DCA-3P ($hX4^{DCA\text{-}3P}$, purple). No significant conformational differences were observed in the overall structures. **b**, Comparison of extracellular and intracellular regions across $hX4^{HEP\text{-}50768}$, $hX4^{MS47134}$, $hX4^{Fospropofol}$, and $hX4^{DCA\text{-}3P}$. While the intracellular sides remain largely unchanged, apparent conformational shifts were observed in ECL1, ECL1, and ECL2, as indicated by the red arrows.

https://doi.org/10.1038/s41589-026-02195-0

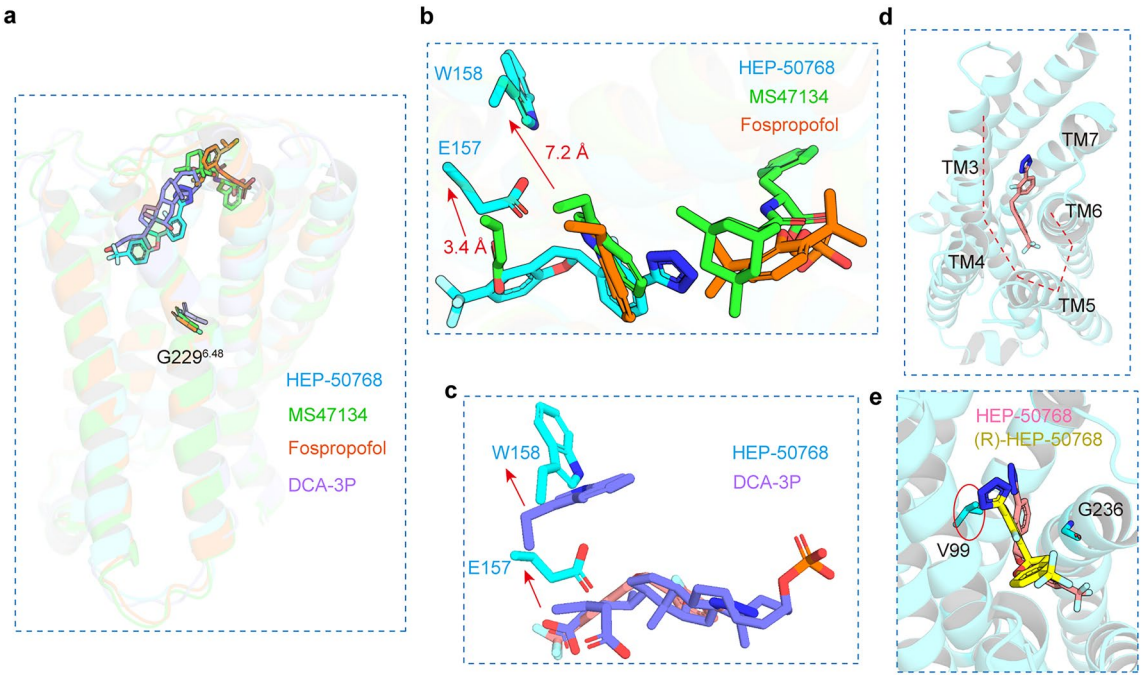

Extended Data Fig. 4 | Binding pocket alignment of hX4$^{HEP-50768}$ and agonists-bound hX4. a, Binding pose comparison among HEP-50768, DCA-3P, MS47134, and Fospropofol. HEP-50768 and DCA-3P inserts more deeply and upright within the pocket, closer to G229$^{6.48}$, while other agonists bind closer to the extracellular surface. Ligands are shown as sticks: HEP-50768 (cyan), MS47147 (green), Fospropofol (orange), and DCA-3P (purple). **b-c**, Residues W158 and E157 in hX4$^{HEP-50768}$ flip outward to create space for the accommodation of HEP-50768 compared to hX4^{MS47134} **(b)** and hX4^{DCA-3P} **(c)**. Red arrows indicate conformational changes. **d**, HEP-50768 binds within an "L-shaped" pocket formed by TM3, TM4, TM5, TM6, and TM7. **e**, The binding pocket of HEP-50768 in hX4 favors (S)-enantiomer over (R)-enantiomer.

https://doi.org/10.1038/s41589-026-02195-0

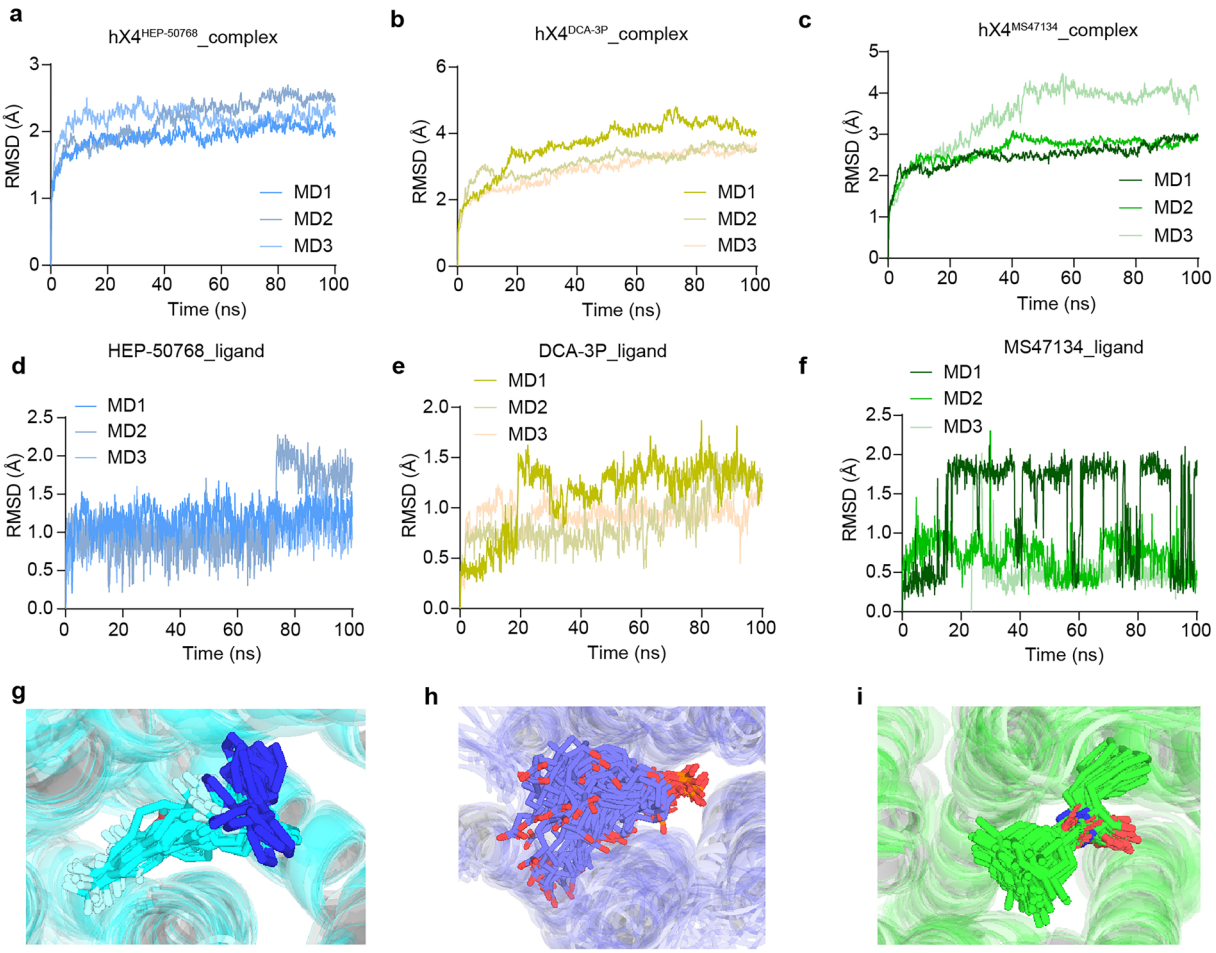

Extended Data Fig. 5 | Three-independent 100 ns MD simulations of hX4$^{HEP-50768}$, hX4^{MS47134} and hX4^{DCA-3P}. a-c, RMSD of hX4$^{HEP-50768}$ **(a)**, hX4^{DCA-3P} **(b)** and hX4^{MS47134} **(c)** complexes during MDs. **d-f**, RMSD of ligand HEP-50768 **(d)**, DCA-3P **(e)** and MS47134 **(f)**. **g-i**, Overlaid MD trajectory of hX4$^{HEP-50768}$ (cyan) **(g)**, hX4^{DCA-3P} (purple) **(h)**, hX4^{MS47134} (green) **(i)**. All the ligand was stabilized in the corresponding binding pocket during MD trajectories.

https://doi.org/10.1038/s41589-026-02195-0

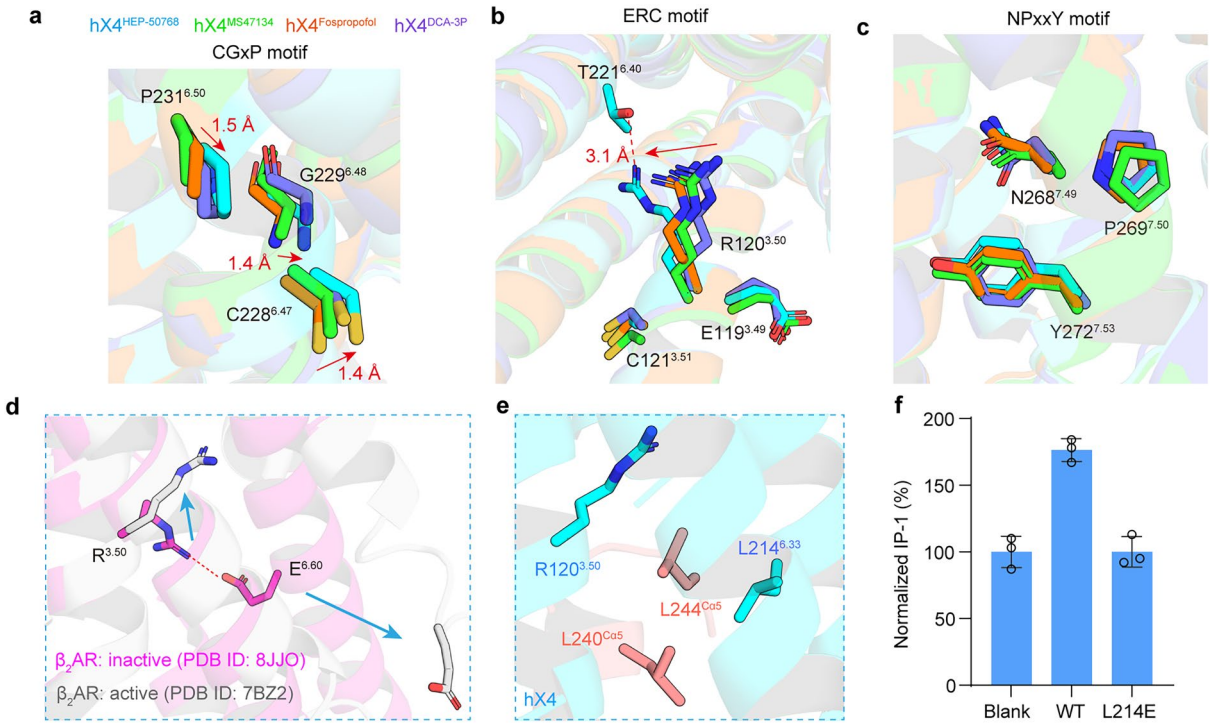

Extended Data Fig. 6 | Structural basis of hX4's constitutive activity and HEP-50768's inverse agonism. a-c, Comparison of microswitch motifs CGxP **(a)**, ERC **(b)**, and NPxxY **(c)** between HEP-50768-bound inverse agonist state and agonist-bound states, highlighting distinct conformational features unique to inverse agonism. Residues are shown as sticks: cyan ($hX4^{HEP\text{-}50768}$), green ($hX4^{MS47147}$), orange ($hX4^{Fospropofol}$), and purple ($hX4^{DCA\text{-}3P}$). Red arrows indicate conformational changes. **d**, In β_2AR, $R^{3.50}$ and $E^{6.30}$ form a salt bridge that lock TM3 and TM6 in the inactive state, these residues rearrange upon activation. Residues are shown as sticks: inactive state (red), active state (grey). Blue arrows indicate conformational changes. **e**, In hX4, the position corresponding to $E^{6.30}$ is occupied by L214, which abolishes the salt bridge. Instead, L214 engages in hydrophobic interactions with L240 and L244 in the G protein, facilitating hX4-G protein coupling. Residues are shown as sticks: hX4 (cyan), G protein (pink). **f**, Mutation of L214 to Glu abolishes the basal activity, suggesting that L214 is critical for hX4's constitutive activity. All plots are representative of three biologically independent experiments, with each experimental data point collected with three technical replicates. Data are shown as mean ± SEM.

https://doi.org/10.1038/s41589-026-02195-0

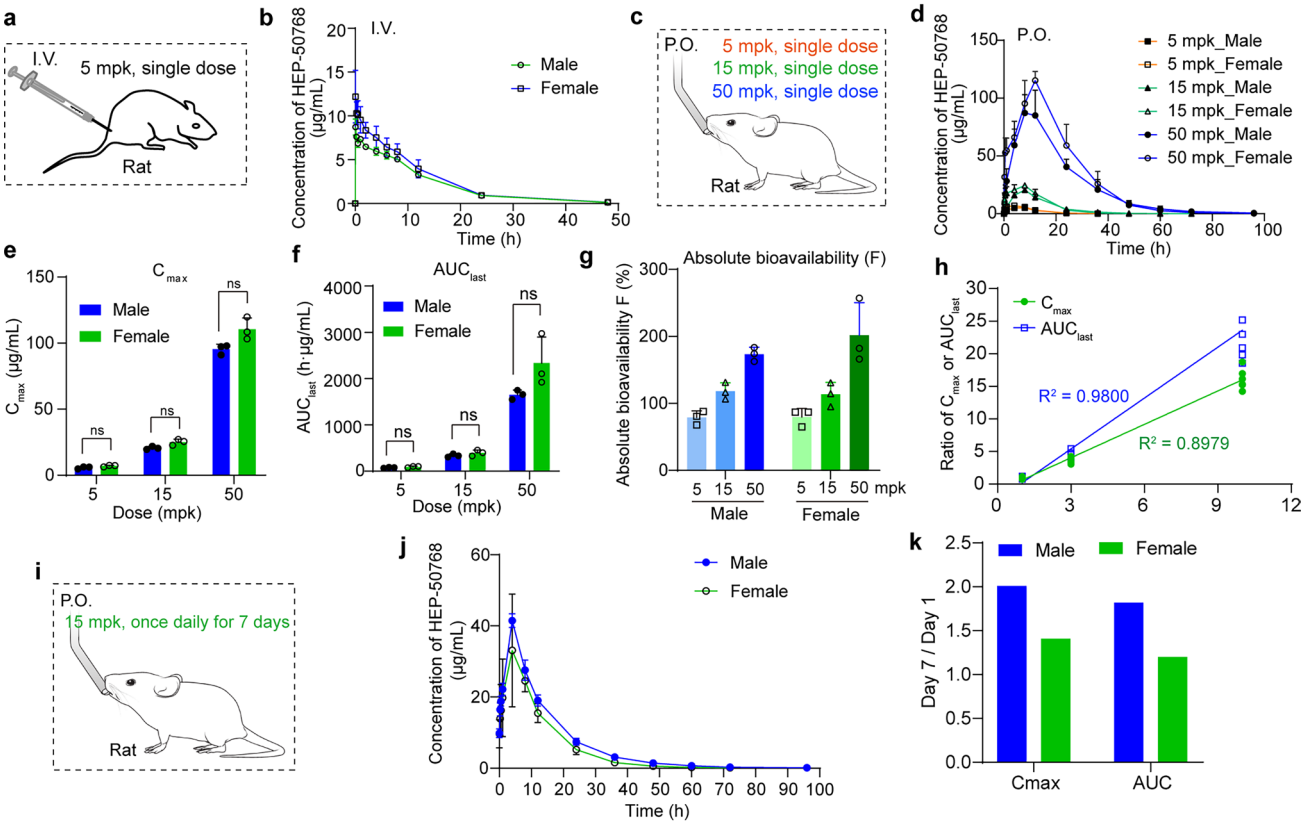

Extended Data Fig. 7 | Pharmacokinetics study of HEP-50768 in SD rats. **a**, Schematic overview of the pharmacokinetics study design in SD rats via intravenous administration. Animals received a single intravenous (I.V.) dose of 5 mg/kg (mg/kg). n = 6 per group (3 males and 3 females). **b**, Plasma drug concentration-time profiles following I.V. **c**, Schematic overview of the pharmacokinetics study design in SD rats via oral administration. Animals were divided into three groups: Group 1 received a single oral dose of 5 mg/kg, Group 2 received a single oral dose of 15 mg/kg, and Group 3 received a single oral dose of 50 mg/kg, respectively. n = 6 per group (3 males and 3 females). **d**, Plasma drug concentration-time profiles following oral administration. **e**-**f**, The peak concentration (Cmax) (**e**) and the systemic exposure (AUClast) (**f**) of male and female rats in different doses. No sex-related differences were observed in either parameter. Data were statistically analyzed by two-sided unpaired t test. "ns" indicates "no significant difference" ($p > 0.05$). **g**, Absolute oral bioavailability of HEP-50768 in SD rats. **h**, Oral administration of 5, 15, and 50 mg/kg resulted in greater-than-dose-proportional increases in both Cmax and AUClast. **i**, Schematic of the 7-day repeated-dose study in SD rats. Animals received 15 mg/kg HEP-50768 orally once daily. n = 6 per group (3 males and 3 females). **j**, Day 7 plasma drug concentration-time profile of HEP-50768 following repeated daily dosing at 15 mg/kg. **k**, Comparable Cmax and AUClast on Day 7 and Day 1 indicated minimal accumulation upon repeated dosing. Data are shown as mean ± SEM. Both male and female rats were included in all groups.

https://doi.org/10.1038/s41589-026-02195-0

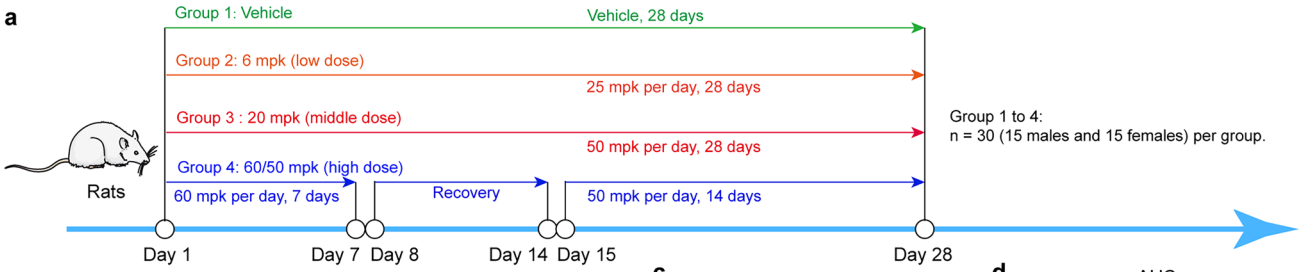

b

	Gender	Dose	$t_{1/2}$ (h)	T_{max} (h)	C_{max} (μg/mL)	$AUC_{0\text{-}24\ h}$ (h·μg/mL)	AUC_{last} (h·μg/mL)
Day 1	Male	6 mpk	8.44	4.00	7.68	112.41	112.41
		20 mpk	-	10.00	31.46	546.73	546.73
		60 mpk	-	12.00	123.04	2309.60	2309.60
	Female	6 mpk	7.02	4.00	8.08	116.55	116.55
		20 mpk	9.74	8.00	36.84	614.04	614.04
		60 mpk	-	10.00	151.13	2278.91	2278.91
Day 15	Male	50 mpk	16.31	8.00	99.67	1650.37	1650.37
	Female	50 mpk	-	10.00	109.01	2013.19	2013.19
Day 28	Male	6 mpk	12.85	8.00	13.91	245.60	365.18
		20 mpk	14.09	8.00	64.65	1175.46	1810.46
		50 mpk	10.00	8.00	168.70	2598.07	3886.88
	Female	6 mpk	10.44	4.00	14.00	220.54	292.91
		20 mpk	11.69	4.00	60.22	1137.46	1605.12
		50 mpk	7.67	10.00	147.91	2483.66	3165.12

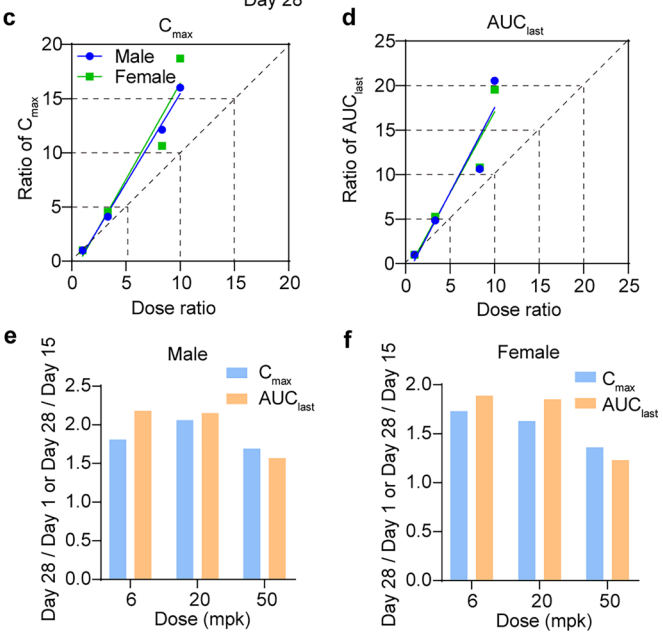

Extended Data Fig. 8 | Toxicity assessment of HEP-50768 in SD rats. **a**, Schematic overview of a 4-week repeated-dose toxicity study of HEP-50768 in SD rats. Animals were divided into 4 groups: Group 1 (n = 10 per group, 5 males and 5 females) received vehicle (water) as control; Groups 2-4 (n = 20 per group, 10 males and 10 females) received oral doses of 6 mpk (low dose), 20 mpk (middle dose) and 60/50 mpk (high dose), respectively. **b**, Summary of toxicokinetic parameters of HEP-50768 across all dosing groups in rats. **c**-**d**, Oral administration of 6, 20, and 60/50 mg/kg resulted in greater-than-dose-proportional increases in Cmax (**c**) and AUClast (**d**) on Day 28. **e**-**f**, Comparable Cmax and AUClast on Day 28 versus Day 1 (for dose of 6 mpk and 20 mpk) or Day 28 versus Day 15 (for dose of 60 mpk) in males (**e**) and females (**f**) indicated minimal accumulation. Data are shown as mean ± SEM.

nature portfolio

Corresponding author(s): Xiaoguang Lei

Last updated by author(s): Feb 25, 2026

Reporting Summary

Nature Portfolio wishes to improve the reproducibility of the work that we publish. This form provides structure for consistency and transparency in reporting. For further information on Nature Portfolio policies, see our Editorial Policies and the Editorial Policy Checklist.

Statistics

For all statistical analyses, confirm that the following items are present in the figure legend, table legend, main text, or Methods section.

n/a	Confirmed
☐	☒ The exact sample size (*n*) for each experimental group/condition, given as a discrete number and unit of measurement
☐	☒ A statement on whether measurements were taken from distinct samples or whether the same sample was measured repeatedly
☐	☒ The statistical test(s) used AND whether they are one- or two-sided *Only common tests should be described solely by name; describe more complex techniques in the Methods section.*
☒	☐ A description of all covariates tested
☐	☒ A description of any assumptions or corrections, such as tests of normality and adjustment for multiple comparisons
☐	☒ A full description of the statistical parameters including central tendency (e.g. means) or other basic estimates (e.g. regression coefficient) AND variation (e.g. standard deviation) or associated estimates of uncertainty (e.g. confidence intervals)
☐	☒ For null hypothesis testing, the test statistic (e.g. *F*, *t*, *r*) with confidence intervals, effect sizes, degrees of freedom and *P* value noted *Give P values as exact values whenever suitable.*
☒	☐ For Bayesian analysis, information on the choice of priors and Markov chain Monte Carlo settings
☒	☐ For hierarchical and complex designs, identification of the appropriate level for tests and full reporting of outcomes
☒	☐ Estimates of effect sizes (e.g. Cohen's *d*, Pearson's *r*), indicating how they were calculated

Our web collection on statistics for biologists contains articles on many of the points above.

Software and code

Policy information about availability of computer code

Data collection	EPU software was used for cryo-EM image collection; FLIPR Tetra system was used for FLIPR data collection; AmberTool was used for molecular dynamic simulaitons.
Data analysis	cryoSPARC, ChimeraX-1.2.5, Coot-0.9.4, Phenix-1.18.2, Molprobity, PyMOL-3.0.4, Graphpad Prism 8, Adobe Illustrator CS6, WinNonlin-8.3.5.340

For manuscripts utilizing custom algorithms or software that are central to the research but not yet described in published literature, software must be made available to editors and reviewers. We strongly encourage code deposition in a community repository (e.g. GitHub). See the Nature Portfolio guidelines for submitting code & software for further information.

Data

Policy information about availability of data

All manuscripts must include a data availability statement. This statement should provide the following information, where applicable:

- Accession codes, unique identifiers, or web links for publicly available datasets
- A description of any restrictions on data availability
- For clinical datasets or third party data, please ensure that the statement adheres to our policy

All the data generated in this study are available in the paper and the Supplementary Information. All the materials needed to replicate the work are available. Cryo-

EM data of HEP-50768-bound MRGPRX4-Gq complex have been deposited at PDB and EMDB with 9V81 and EMD-64829 respectively. Cryo-EM data of local refined structure of HEP-50768-bound MRGPRX4 have been deposited at PDB and EMDB with 9V82 and EMD-64830 respectively.

Research involving human participants, their data, or biological material

Policy information about studies with human participants or human data. See also policy information about sex, gender (identity/presentation), and sexual orientation and race, ethnicity and racism.

Reporting on sex and gender	The study did not involve human participants or human data.
Reporting on race, ethnicity, or other socially relevant groupings	N/A
Population characteristics	N/A
Recruitment	N/A
Ethics oversight	N/A

Note that full information on the approval of the study protocol must also be provided in the manuscript.

Field-specific reporting

Please select the one below that is the best fit for your research. If you are not sure, read the appropriate sections before making your selection.

☒ Life sciences ☐ Behavioural & social sciences ☐ Ecological, evolutionary & environmental sciences

For a reference copy of the document with all sections, see nature.com/documents/nr-reporting-summary-flat.pdf

Life sciences study design

All studies must disclose on these points even when the disclosure is negative.

Sample size	No statistical methods used to predetermine sample size. For the cryo-EM study, the number of micrographs is determined by the available microscope time. For all inhibition assays and animal experiments were performed in triplicate or more, which were sufficient to support the conclusions. Sample sizes are indicated in the respective Methods and figure legends. Data were analyzed by fitting various ligand concentrations and readouts using appropriate equations in GraphPad Prism 8.
Data exclusions	No data was excluded.
Replication	Each experiments were replicated at least 3 times and described in the manuscript. All attempts at replication were successful.
Randomization	For animal experiments, rats and monkeys were always randomly assigned into different groups, For the rest studied, randomization was not relevant, as the independent variables were sufficient for the interpretation within this study.
Blinding	For animal experiments, the investigators were blinded to group allocation during both data collection and analysis. For cryo-EM structure determination and other functional studied, blinding is not necessary due to the nature of these experiments do not requires subject assessment of the data that may influence the validity of the results.

Reporting for specific materials, systems and methods

We require information from authors about some types of materials, experimental systems and methods used in many studies. Here, indicate whether each material, system or method listed is relevant to your study. If you are not sure if a list item applies to your research, read the appropriate section before selecting a response.

Materials & experimental systems

n/a	Involved in the study
☒	☐ Antibodies
☐	☒ Eukaryotic cell lines
☒	☐ Palaeontology and archaeology
☐	☒ Animals and other organisms
☒	☐ Clinical data
☒	☐ Dual use research of concern
☒	☐ Plants

Methods

n/a	Involved in the study
☒	☐ ChIP-seq
☒	☐ Flow cytometry
☒	☐ MRI-based neuroimaging

Eukaryotic cell lines

Policy information about cell lines and Sex and Gender in Research

Cell line source(s)	Sf9 insect cells (Invitrogen, USA), HEK293T cell lines (Gibco, USA).
Authentication	Cell lines were not authenticated.
Mycoplasma contamination	All cell lines were negative for mycoplasma contamination.
Commonly misidentified lines (See ICLAC register)	Commonly misidentified lines were nor used in this study.

Animals and other research organisms

Policy information about studies involving animals; ARRIVE guidelines recommended for reporting animal research, and Sex and Gender in Research

Laboratory animals	Sprague-Dawley (SD) rats; Rhesus monkeys
Wild animals	The study did not involve wild animals.
Reporting on sex	For pharmacokinetic and toxicity study of HEP-50768, male rats (7-8-week-old, 236 to 278 g) and female rats (7-8-week-old, 218 to 250 g) were used for all animal experiments.Male monkeys (2.5 to 8-year-old, 5.10 to 9.28 kg) and female monkeys (2.5 to 8-year-old, 2.96 to 5.32 kg) were used for all animal experiments.
Field-collected samples	Rats were group-housed (3-5 animals per cage) under a standard 12-hour light/ 12-hour dark cycle, and all behavioral experiments were performed during the light cycle. For monkeys, they were housed under a standard 12-hour light/ 12-hour dark cycle. And male adaptive feeding for 7 days and female adaptive feeding for 13 days before conducting experiments.
Ethics oversight	All animal experiments were approved by the Animal Care and Use Committee of Peking University of Life Science.

Note that full information on the approval of the study protocol must also be provided in the manuscript.

Plants

Seed stocks	The study did not involve plants.
Novel plant genotypes	The study did not involve plants.
Authentication	N/A.